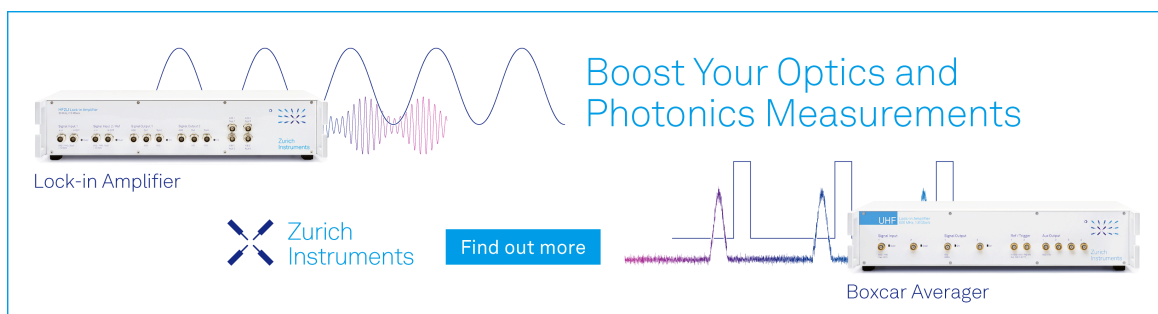# Ultrafast control of laser-induced spin-dynamics scenarios on two-dimensional $Ni_3@C_{63}H_{54}$ magnetic system

Mohamed Barhoumi [ID] ; Jing Liu [ID] ; Georgios Lefkidis [✉] [ID] ; Wolfgang Hübner [ID]

Check for updates

View Online

Export Citation

Ultrafast control of laser-induced spin-dynamics scenarios on two-dimensional Ni₃@C₆₃H₅₄ magnetic system

View Online   Export Citation   CrossMark

Mohamed Barhoumi,[1,a)] (iD) Jing Liu,[2,b)] (iD) Georgios Lefkidis,[1,c)] (iD) and Wolfgang Hübner[1,d)] (iD)

AFFILIATIONS

[1] Department of Physics, Rheinland-Pfälzische Technische Universität Kaiserslautern (RPTU) Kaiserslautern-Landau, P.O. Box 3049, 67653 Kaiserslautern, Germany
[2] Institute of Theoretical Chemistry, Ulm University, 89081 Ulm, Germany

a) Electronic mail: mbarhou@rptu.de
b) Electronic mail: jing-1.liu@uni-ulm.de
c) Author to whom correspondence should be addressed: lefkidis@rptu.de
d) Electronic mail: huebner@rptu.de

ABSTRACT

The concept of building logically functional networks employing spintronics or magnetic heterostructures is becoming more and more popular today. Incorporating logical segments into a circuit needs physical bonds between the magnetic molecules or clusters involved. In this framework, we systematically study ultrafast laser-induced spin-manipulation scenarios on a closed system of three carbon chains to which three Ni atoms are attached. After the inclusion of spin–orbit coupling and an external magnetic field, different ultrafast spin dynamics scenarios involving spin-flip and long-distance spin-transfer processes are achieved by various appropriately well-tailored time-resolved laser pulses within subpicosecond timescales. We additionally study the various effects of an external magnetic field on spin-flip and spin-transfer processes. Moreover, we obtain spin-dynamics processes induced by a double laser pulse, rather than a single one. We suggest enhancing the spatial addressability of spin-flip and spin-transfer processes. The findings presented in this article will improve our knowledge of the magnetic properties of carbon-based magnetic molecular structures. They also support the relevant experimental realization of spin dynamics and their potential applications in future molecular spintronics devices.

I. INTRODUCTION

The need for computer processor downsizing is rising in the present. Single molecules and nanoparticles are two examples of nanoscale materials that are gaining greater and greater interest.[1–6] These systems, i.e., single molecules and nanoparticles, have a significant deal of promise as candidates for future spin logic devices[7–13] due to their extraordinary physical properties, such as discrete levels and high spin localization, which enable the controllable spin and magnetic processing. The features of genuine logical devices can be instantly, accurately achieved and anticipated by quantum chemistry computations.[14–19] In this pathway, many works made one step forward to scrutinize short and long spin-dynamics

(spin-flip, spin-transfer, etc.)[20–22] processes. For instance, Hübner et al. provided nickel (Ni₂) dimer-based quantum heat machines in which they accomplished comprehensive *ab initio* computations, incorporating spin–orbit coupling (SOC) and electronic correlation.[23] Koopmans et al. presented a microscopic prototype that successfully demonstrates the ultrafast equilibration of magnetic order in ferromagnetic metals.[24] Gómez-Abal et al.[25] put up a theory that spin–orbit coupling combined with correctly structured femtosecond (fs) laser pulses leads to ultrafast all-optical magnetic flipping. Spin dynamics is at the core of spin technology and spin-based quantum technology. At present, theoretical methods can predict spin dynamics on molecular systems and clusters with high accuracy. Among these methods, we underline quantum optimal control

29 April 2024 13:08:03

theory (QOCT),[26] which represents a collection of methods to design and implement shapes of external electromagnetic fields for controlling quantum dynamical processes at the atomic or molecular scale.[27] For example, QOCT is employed to create logical qubits encoded in bosonic modes[28] and to implement quantum gates.[29–31] Moreover, spin-flip and spin-transfer on double-magnetic-center graphene nanoflakes are examined with quantum chemical calculations by Zhang et al.[32,33] Recently, Sold et al. have offered an integrated experimental and theoretical investigation of the ultrafast transient absorption spectroscopy outcomes of Ni_2Dy_2, a compound in dimethylformamide (DMF), which can be considered as a model molecule for single-molecule magnets.[34,35] Ab initio calculations were employed to achieve quantum control by studying the ultrafast spin switching and related strain effect on Co-doped endohedral fullerenes.[36] The spin-transfer scenarios are used to build an all-spin OR gate.[2] Applying highly correlated quantum chemical simulations, Xu et al.[37] computationally examined the strain modification of ultrafast spin-flip processes on $Ni@B_{80}$ endohedral fullerene. Fe_3GeTe_2 has been proposed[38] as a promising substance for layered two-dimensional (2D) heterostructure spintronic devices. In an effort to measure magnon currents on the magnetic configuration of the object, spin-valve structures depending on a set of ferromagnets were created.[39] Investigations on spin processes in molecules with three magnetic centers have been extensive.[40,41] The diamond-based substance exhibits high interactions between charge transport, spin, and the magnetic field, making spintronic applications available.[42] Liu et al. described an optically induced subpicosecond spin-transfer scenario over 4.428 nm, which is substantially similar to the real Complementary Metal Oxide Semiconductor (CMOS) size, employing a high-level ab initio quantum method.[43] In addition, Liu et al. systematically investigated the spin-dynamics processes on two different carbon cross arrangements with two Ni atoms attached.[44] Recently, Liang et al.[45] have studied the laser-induced ultrafast spin dynamics in four trigonal monopyramidal complexes. They created many reversible spin-crossover processes and mixed scenarios of charge transfer and spin bifurcation under the usage of various well-tailored laser pulses. Despite there being many published results[44,46–54] on semiconductors and magnetic molecules to build logic devices, the incorporation of magnetic molecules in useful device applications is still poor. The two biggest challenges to building spin-based devices are discovering molecular systems and incorporating those elements into the building blocks of spintronic heterostructures.[55] The quest for appropriate molecular systems with the preferred functionalities on ultrafast timescales is an active field. Moreover, alternative ultrafast and ultrasmall technologies are growing increasingly in demand as the capacity of conventional semiconductor-based logic elements approaches saturation. In addition, quantum integrated circuits (ICs) are based on logical functionalities, which are built using magnetic elements or spintronics. In this investigation, the creative idea of spin-based logic functionality is presented. Our main emphasis is on the ultrafast control of laser-induced spin-dynamics scenarios on the two-dimensional $Ni_3@C_{63}H_{54}$ magnetic system. Established on the high-level computation of the ground and excited states of this many-body system, after the inclusion of spin–orbit coupling (SOC)[56] and an external magnetic field, a variety of ultrafast spin dynamics scenarios, involving spin-flip and long-distance spin-transfer processes has been achieved by various appropri-

ately well-tailored time-resolved laser pulses within subpicosecond time-scales.

Generally, a molecular system requires magnetic centers to perform logical processes. Signal transport is already possible between two magnetic centers, and interference features could be added between three centers. Our $Ni_3@C_{63}H_{54}$ realistic molecular system is cut out of a graphene monolayer,[57–59] with hydrogen atoms saturating the bonds wherever necessary, and the benzenes are chosen in order to create a chemically correct flat structure. Furthermore, several ingredients of our envisaged system, such as graphene monolayers, carbon clusters,[60] carbon chain radical anions,[61] neutral carbon chains,[62] carbon ring chains,[63] and other related systems,[64] have been synthesized. Our molecular system is a derivative of graphene and belongs to these carbon system classes. The idea of using polyacetylene chains to connect the magnetic centers over large distances stems from cutting stripes out of graphene sheets.[65–68] The reason is that while intermetallic connectivity through s orbitals (e.g., metallic Na[69]) does not allow for the long-distance spin transfer, the conjugated p_z bonds in graphene do.[43,44] Much progress has been reported lately in the fabrication of doped and freestanding or ordered polyacetylene chains.[70–79] Thus, guided by the experimental design, our $Ni_3@C_{63}H_{54}$ molecular system can be achieved.[80–82]

The present article is an essential part of our systematic investigations regarding our vision to realize integrated nanospintronic circuits and deals with the connectivity of magnetic centers, as well as the impact of the spin-transfer channels on their possible quantum control. In addition, since magnetic elements are the most promising adatoms of different carbon-including nano-structures, for magnetic functionalization, we use nickel (Ni) atoms. This paper is organized in the following way: In Sec. II, we give a quick outline of the theory and the methods, which are employed to study spin dynamics. Then, in Sec. III, we deliver our results regarding spin-dynamics processes and the influence of the orientation of the laser pulse on spin-flip and spin-transfer scenarios. Finally, we conclude in Sec. V.

II. COMPUTATIONAL METHOD AND THEORY

We achieve uncorrelated molecular orbitals (MOs) at the restricted open-shell Hartree–Fock (ROHF) level[83,84] to calculate the electronic states. In addition, we employ the equation-of-motion coupled-cluster method with single and double virtual excitations (EOM-CCSD)[85,86] together with the 6-31G basis set, which is implemented in the GAMESS software package.[87] Then, we combine the high-level quantum chemistry theory EOM-CCSD with the Lambda (Λ) process[12,88] to investigate the spin-flip and spin-transfer scenarios in our system. In this way, spin–orbit coupling and an external magnetic field B are required.[89–91] Note that in a spin-flip process, the initial and target states have opposite spin orientations. The population must be transferred from the initial state to the final state via spin-mixed intermediate states because direct excitations between two states with opposite spin orientations are prohibited. In our situation, we use 1.0×10^{-8} a.u. as a magnetic field strength, and SOC yields the spin-mixing of the intermediate state. Spin-flips require spin-mixed intermediate states, which have to be connected to both spin-up (α) and spin-down (β) states. It is important to have significant energy differences in order to appropriately treat

the initial and target states of a lambda process by an external laser pulse. Because the spin-up and spin-down states are frequently degenerate or quasi-degenerate, a Zeeman splitting between them must be generated by an external magnetic field. That means a static external magnetic field of 1.0×10^{-8} a.u. is used to distinguish between spin-up and spin-down states and create spin-mixed intermediate states that allow for the indirect transition between the initial and final states as needed by the process. The magnetization direction is also controlled by the external magnetic field. The many-body wave functions computed with EOM-CCSD and an external magnetic field are formed perturbatively with the related Hamiltonian

$$\hat{H}^{\text{SOC+B}} = \sum_{i=1}^{n} \frac{Z_a^{\text{eff}}}{2c^2 R_i^3} \hat{\mathbf{L}} \cdot \hat{\mathbf{S}} + \mu_L \hat{\mathbf{L}} \cdot \mathbf{B}_{\text{stat}} + \mu_{\mathbf{S}} \hat{\mathbf{S}} \cdot \mathbf{B}_{\text{stat}}. \quad (1)$$

$\hat{\mathbf{L}}$ and $\hat{\mathbf{S}}$ are the orbital and spin momentum operators, respectively, μ_L and μ_S are their gyromagnetic ratios, and c is the speed of light. The magnitude of the position vector of the ith electron and the static external magnetic field are R_i^3 and $\mathbf{B}_{\text{stat}}$, respectively. Z_a^{eff} represents the relativistic effective nuclear charges of the ath atom (effectively accounting for the two-electron contributions) required for the SOC. Subsequently, the system's many-body wave function is reproduced in time under the influence of a laser pulse,

$$\frac{\partial c_n(t)}{\partial t} = \frac{-i}{\hbar} \sum_k \langle \Phi_n | \hat{H}(t) | \Phi_k \rangle c_k(t) e^{-\frac{i}{\hbar}(E_k - E_n)t}. \quad (2)$$

The unperturbed eigenstates received from EOM-CCSD calculations are Φ_n and Φ_k. E_n and E_k are the energies of Φ_n and Φ_k, respectively. c_n is the complex scalar coefficient of state Φ_n. $\hat{H}(t)$, which is the Hamiltonian describing the impact of the time-dependent laser pulse, is given by

$$\hat{H}(t) = \hat{\mathbf{D}} \cdot \mathbf{E}_{\text{laser}}(t). \quad (3)$$

$\hat{\mathbf{D}}$ and $\mathbf{E}_{\text{laser}}$ are the electric dipole transition operator and the electric field, respectively. Equation (2) is propagated with an embedded fifth-order Runge–Kutta method associated with the Cash–Karp adaptive-step size.[92] Quantum optimal control theory, quantum feedback control,[93] and machine learning[94] are used to study the quantum processes. In our case, for the laser parameters, we employ a specially developed genetic algorithm.[69,95] As the numerical optimal control algorithms,[96] in our genetic algorithm, no experimental input is necessary. Our genetic algorithm has been successfully employed in many systems in the past; it is highly parallelized and incorporates analytical filters, which exclude unsuccessful laser-pulse combinations. In optimization computations, eight parameters are considered: the angles of incidence in spherical coordinates θ and ϕ (ranging from 0° to 180° and 0°–360°), the angle γ between the polarization of light and the optical plane, the ellipticity β, the full width at half-maximum (FWHM) of the laser pulse (ranging from 0 to 500 fs), the laser energy E_{laser}, the amplitude of the laser pulse, and the chirp (chosen between -5% and $+5\%$). The genetic algorithm treats each laser pulse as a separate individual, with the eight parameters working as the individual's genes. The best genes (which produce higher fidelity) are selected and passed on to the next generation by applying suitable genetic operations (such as gene crossing and mutation). As a result, the parameters are improved

globally, and the best genes evolve. The fidelity is described as the population of the final state after the impact of the laser pulse. Note that each generation includes 200 individuals, and the optimization typically requires 200 generations.

III. RESULTS AND DISCUSSION

We start by representing our geometric configuration of the $Ni_3@C_{63}H_{54}$ carbon-based material, which is sketched in Fig. 1. Our system is merely a closed structure formed by three carbon chains connected by three benzenes and with three Ni atoms attached [as displayed in Fig. 1(a)]. In this $Ni_3@C_{63}H_{54}$ molecular system, the C–C bond length is always identical to the length of the C–C bond of graphene, which is 1.42 Å. The distance between the Ni1 and Ni2 atoms is 27.14 Å. This length is identical to the distance between Ni1 and Ni3 (or between Ni2 and Ni3). The angle between the two C–C bonds is designated at 120°. In addition, the C–H bond length and the angle between C–H and the C–C bond are maintained at 1.090 Å and 120°, respectively. Note that the honeycomb-like edges of bare finite graphene exhibit spin polarization,[97] which already makes them desirable as components for spintronic devices. In addition, ideal spin filters with almost 100% spin polarization are created by connecting carbon atomic chains to graphene electrodes.[98] Thus, since one of our main objectives here is to study the long-distance ultrafast spin transfer between the spin centers (Ni atoms) for building and supporting spin-logic units for developing future all-optical magnetic unit operations, therefore, we use as a backbone structure a chain carbon system.[43,44] Furthermore, the choice of triangular systems has the advantage, which, besides spin-flip (one center needed) and spin-transfer (two centers needed), contains enough complexity to also perform spin-bifurcation, spin-merging, and spin-bounce operations.[2,40,41,99] These can give rise to classical-Boolean or even quantum-logic operations.[35,100,101] Ideally, the three magnetic centers should consist of the same atoms, but with slightly different local symmetries, so that they become energetically distinguishable (and thus individually addressable) and exhibit spin-density localization, while still interacting with each other.[100,102] In particular, monodisperse bare Ni_3 nanoislands are experimentally feasible[103] as adsorbates. Therefore, our triangular prototypic system represents an ideal minimal structure to study integrated magnetic logic circuits. Our system has C_s symmetry, which is a subgroup of the symmetry group C_{3v} since we connect the three Ni atoms asymmetrically. The left, right, and top atoms are identified as Ni2, Ni3, and Ni1, respectively, to make them easy to distinguish. We show some molecular orbitals (MO_{257}, MO_{258}, MO_{259}, and MO_{260}), including the highest occupied molecular orbital (HOMO) and lowest unoccupied molecular orbital (LUMO) of $Ni_3@C_{63}H_{54}$ in Figs. 1(b)–1(e). MO_{257} (HOMO-1), which serves as an intermediate MO for the direct Ni1 and Ni2 (Ni1 → Ni3 or Ni2 → Ni3) transfer, is appearing on the carbon atoms with an energy of $-0.125\,90$ eV and the dominant atomic orbital is p_z. In addition, the highest occupied molecular orbital (MO_{258}, HOMO) is located at the carbon atoms with the same energy ($-0.125\,90$ eV) and the dominant atomic orbital is p_z. However, the atomic orbitals s, p_x, d_{xx}, d_{xy}, and d_{zz} of Ni1 make up the lowest unoccupied molecular orbital (MO_{259}, LUMO). MO_{260} (LUMO + 1) is located on Ni2 with an energy of $-0.071\,70$ eV, and the dominant atomic orbitals are s, p_x, p_y, d_{xy}, and d_{yy} [see Fig. 1(e)]. To achieve the spin-flip and spin-transfer (see Sec. IV)
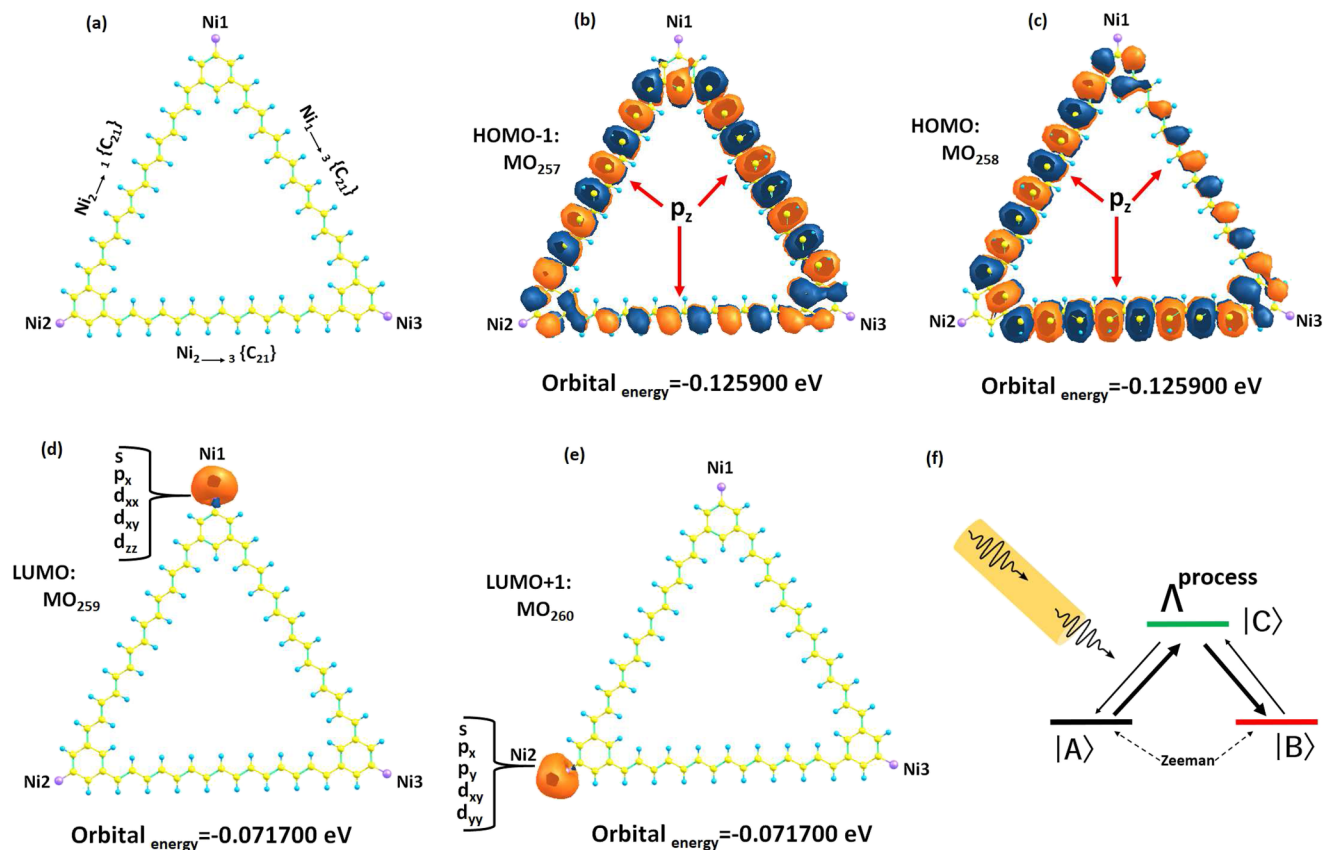
FIG. 1. (a) A closed system of three carbon chains with three nickel atoms attached ($Ni_3@C_{63}H_{54}$). The number of carbon atoms between two Ni atoms is 21 atoms, and the total number of atoms used is 120 atoms. (b) Molecular orbital MO_{258} with energy $-0.125\,90$ eV. (c) Highest occupied molecular orbital (HOMO). (d) Lowest unoccupied molecular orbital (LUMO). (e) Molecular orbital MO_{260} with energy $-0.071\,70$ eV. (f) The spin-dynamics processes are achieved under a single (or double) laser pulse using Λ processes ($|A\rangle$, $|C\rangle$, and $|B\rangle$ are the initial, intermediate, and final states, respectively. A Zeeman splitting between the initial and target states must be generated by an external magnetic field. Note that the yellow, blue, and purple spheres are carbon, hydrogen, and nickel atoms, respectively.

on our system, we employ the Λ process (theory for the three-level system), which is depicted in Fig. 1(f). We designate the three states by $|A\rangle$ (initial state), $|B\rangle$ (target state), and $|C\rangle$ (intermediate state). Our purpose is to transfer the population from state $|A\rangle$ to $|B\rangle$. If the population transfer occurs via the third state $|C\rangle$, this is named a Lambda (Λ) process, which has been successfully employed in previous quantum chemical computations,[104] e.g., Jin *et al.* studied theoretical and experimental investigation of the optical properties and dynamics of the two-magnetic-center compound $[Ni_2^{II}(L\text{-}N_4Me_2)(emb)]$.[55] In this kind of process, we have $E_{|A\rangle} \neq E_{|B\rangle} < E_{|C\rangle}$, where $E_{|A\rangle}$, $E_{|B\rangle}$, and $E_{|C\rangle}$ are the energies of the initial, target, and intermediate states, respectively. If the population transfers from the initial state $|A\rangle$ to the desired target state $|B\rangle$, then the system is called controllable. The energy levels of the states before and after involving SOC and magnetic field are displayed in Fig. 2. We receive various spin states of a multiplet that are degenerate. In addition, to lift the degeneracy, we include SOC and a static magnetic field. A noticeable point that is SOC in transition metals provides a considerable

part in significant observables as zero-field splitting and line contours of electron resonance ranges.[105–107] In our case, the many-body states are eigenstates of the S^2 operator when the magnetic field and SOC are absent (as illustrated in Fig. 2). Any linear combination of the states is also an eigenstate of the overall Hamiltonian, and α and β states continue to be degenerate. Consequently, we are unable to differentiate between spin-up and spin-down states. Even with the addition of SOC, the situation does not change (Kramers' theorem). Thus, to produce states with distinct spin values, a relative magnetic field of 1.0×10^{-8} a.u. is applied. After SOC + B, the new states are no longer eigenstates of the spin operator S^2. The exact spin values S^2 and S_z of the new states cannot be calculated. Nevertheless, quantum mechanical expectation values $\langle S \rangle$ can be obtained and are very near to the pure S values. In our situation, a magnetic field of 1.0×10^{-8} a.u. can give spin expectation values between -0.9999 and 0.9999 for the triplet states. Furthermore, our calculations show that the ground state is a singlet and the first four states also are singlets.
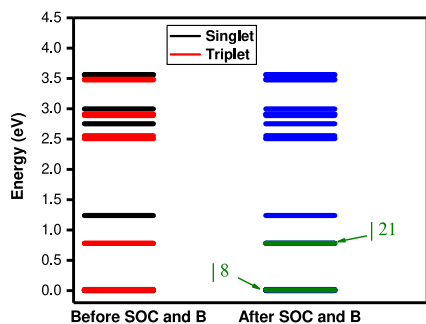
FIG. 2. Low-lying energy level of $Ni_3@C_{63}H_{54}$ without and with SOC and a magnetic field (B = 1×10^{-8} a.u. = 2.35 mT). Black and red are the singlet and triplet states, respectively. Blue and green (initial and target states) are the states after the inclusion of spin–orbit coupling with a static magnetic field.

A. Spin-density distribution

There are several conditions related to the spin density distribution for accomplishing spin-dynamics scenarios on our system. (i) On the Ni elements, there need to exist states with extremely strong localized spin. (ii) The spin density must be distributed unevenly on the Ni atoms. (iii) Then, it must be many states with spin localized on carbon atoms, which can act as intermediate states for the spin-transfer scenario. In our computations, we employ the Mulliken population analysis on the one-electron reduced density matrix to compute the spin density distribution on the carbon system to which the Ni atoms are attached. We provide the density distribution together with expectation values of the spin angular momentum $\langle S_z \rangle$ for some states in Table I. Our calculations are based on the CCSD and EOM-CCSD methods, and the basis set for various elements is 6-31G. We find that Ni3 has the highest spin density with an expectation value of 1.050 at state $|5\rangle$ (the total spin density is 2.0). In addition, the highest absolute value of the spin density distributed on Ni1 and Ni2 is 0.987 ($|23\rangle$) and 1.042 ($|20\rangle$), respectively. The remaining spin density, which has a total value of around 1.00 and is primarily caused by the half-filled conjugated orbitals, is shared by spin-polarized carbon atoms. The delocalized electronic configuration of the states can well explain the spin density distribution. Indeed, the linear combination of various Slater determinants constructed from HF-optimized MOs results in CC many-body wave functions. The other determinants, except the HF reference determinant, involve virtual excitations from the occupied MOs to the empty MOs.[108,109] Here, we analyze the dominant virtual excitation in some states to better understand the spin-density distribution. We take the triplet state $|8\downarrow\rangle \rightarrow |10\uparrow\rangle$ as an example. At the many-body state $|8\downarrow\rangle$, the dominant virtual excitation is from MO_{258} to MO_{260} with an amplitude of 0.529. As we mentioned above, the main atomic orbital contribution to MO_{258} (HOMO) is p_z of carbon atoms, while the atomic orbitals s, p_x, p_y, and d_{xy} of Ni2 contribute to MO_{260}. Therefore, the correlation assisting the transition from MO_{258} to MO_{260} is a p–d excitation. In the state $|10\uparrow\rangle$, the dominant virtual excitation is also from MO_{258} to MO_{260}. MO_{260} is always located at Ni2. This explains the spin density localization on Ni2 of states $|8\downarrow\rangle$ and $|10\uparrow\rangle$. Therefore, a spin-flip process $|8\downarrow\rangle \rightarrow |10\uparrow\rangle$ can be accomplished. The dominant virtual excita-

TABLE I. Energies, spin density distribution on Ni atoms, and expectation values of the spin angular momentum elements for the spin-flip and spin-transfer scenarios on $Ni_3@C_{63}H_{54}$ for the appropriate many-body states with spin–orbit coupling and a static magnetic field (B = 1.0×10^{-8} a.u.) included. The sign of $\langle S_z \rangle$ signifies the spin direction: the positive and negative values are spin-up ↑ and spin-down ↓, respectively. All the calculations are performed with the EOM-CCSD method.

States	E (meV)	$\langle S_z \rangle$	Spin density Ni1	Ni2	Ni3
$|5\rangle$	10.006	−0.996	0.000	0.000	−1.050
$|7\rangle$	10.007	0.996	0.000	0.000	1.050
$|8\rangle$	11.106	−0.495	0.000	−0.523	0.000
$|10\rangle$	11.108	0.495	0.000	0.523	0.000
$|11\rangle$	12.814	−0.529	−0.559	0.000	0.000
$|13\rangle$	12.816	0.529	0.559	0.000	0.000
$|14\rangle$	14.895	−0.893	0.000	0.000	−0.951
$|16\rangle$	14.896	0.893	0.000	0.000	0.951
$|18\rangle$	779.883	−0.998	0.000	−1.042	0.000
$|21\rangle$	782.012	−0.947	−0.987	0.000	0.000
$|23\rangle$	782.013	0.947	0.987	0.000	0.000
$|25\rangle$	2508.235	−0.999	−0.021	−0.026	−0.091
$|27\rangle$	2508.236	0.999	0.021	0.026	0.091
$|31\rangle$	2556.113	−0.998	−0.024	−0.033	−0.048
$|33\rangle$	2556.114	0.998	0.024	0.033	0.048
$|35\rangle$	2887.498	−0.933	−0.275	−0.281	−0.167
$|37\rangle$	2887.499	0.933	0.275	0.281	0.167

tion in the states $|11\downarrow\rangle$ and $|13\uparrow\rangle$ is from MO_{257} to MO_{259}, which is created by the atomic orbitals s, p_x, p_y, d_{xy}, and d_{yy} of Ni1. For this reason, the spin density with an absolute value of 0.559 is localized on Ni1. Thus, a spin-flip process $|11\downarrow\rangle \rightarrow |13\uparrow\rangle$ can be achieved.

We currently possess all the essential knowledge of the new states' attributes. Under the impact of a laser pulse, we propagate the electronic population from one many-body state to another. As mentioned above, the propagation of the wave function is achieved within the interaction picture in the Fock-space traversed by the time-independent Hamiltonian employing a fifth-order Runge–Kutta method and Cash–Karp adaptive step size control. A specially created genetic algorithm is used to optimize the laser pulse parameter. A variety of spin dynamical processes, including spin-flip and spin-transfer, can be designed depending on the spins and localizations of the initial and final states of propagation. In Sec. IV, we discuss each of these spin dynamics scenarios in detail. These scenarios are governed by the interaction of the spins and the laser pulse as determined by the time-dependent version of the celebrated Goodenough–Kanamori rules.[20,110] In all the following scenarios, we include a static magnetic field at $\theta = 0.0°$ and $\phi = 0.0°$ and B = 1.0×10^{-8} a.u. with respect to the molecular axis.

IV. SPIN-FLIP AND SPIN-TRANSFER PROCESSES

Herein, we show that the long-distance spin transfer processes between the three spin centers (Ni atoms) are accomplished along with the local spin-flip mechanism, thus guiding to an improved

functionality. Typically, the initial and target states of the spin-flip process stemming from the same triplet states are quasi-degenerate. They cannot be employed for spin transfer since they are localized on the same atom.

A. Spin-flip scenarios

As aforementioned, in a Λ process, if the initial and final states have the same spin localization and opposite spin direction, then it is a spin-flip process. According to the spin density distribution, different spin-flip scenarios can be accomplished, e.g., $|8 \downarrow\rangle \rightarrow |10 \uparrow\rangle$, $|11 \downarrow\rangle \rightarrow |13 \uparrow\rangle$, and $|18 \downarrow\rangle \rightarrow |20 \uparrow\rangle$. The time-resolved expectation values of the spin components after the effect of the laser pulse on these spin-flip scenarios are investigated. For instance, we show the expectation values of the spin angular momentum element $\langle S_z \rangle$ for the spin-flip processes $|8 \downarrow\rangle \rightarrow |10 \uparrow\rangle$ and $|11 \downarrow\rangle \rightarrow |13 \uparrow\rangle$ in Figs. 3 and 4, respectively. In our calculations, the many-body states are propagated in time under the impact of a sech²-shaped laser pulse. Figures 5 and 6 show the laser pulse envelope shape of field $\frac{E}{E_0}$ = sech²(t) for the local spin-flip scenarios $|8 \downarrow\rangle \rightarrow |10 \uparrow\rangle$ and $|11 \downarrow\rangle \rightarrow |13 \uparrow\rangle$. In the local spin-flip on Ni2, the time-dependent population of each state (initial, target, and intermediate) is depicted in Fig. 7. We choose state $|8 \downarrow\rangle$ [$E_{|8\downarrow\rangle}$ = 11.106 meV; spin is localized on Ni2, black dashed line in the upper panel in Fig. 7(a)] and state $|10 \uparrow\rangle$ [$E_{|10\uparrow\rangle}$ = 11.108 meV; spin is also localized on Ni2, red solid line in the upper panel in Fig. 7(a)] as the initial and final states, respectively. The energy difference is 2.00×10^{-6} eV, which is sufficient to make the two states distinguishable for a laser pulse, indicating the subtle sensitivity of our processes in molecular substances. We note that starting from the state $|8 \downarrow\rangle$ we reach state $|10 \uparrow\rangle$ driven by a single laser pulse with θ = 75.59°, ϕ = 165.87°, γ = 76.37°, β = 106.95°, FWHM = 342.87 fs, the amplitude of the electric field 5.10×10^9 V/m (see Fig. 5), and a chirp of 0.990. In addition, a threshold of 10^{-3} is established for the electronic density's propagation: the amplitude of the electric-dipole transition matrix elements between the states is constrained by this parameter. The fidelity of this process $|8 \downarrow\rangle \rightarrow |10 \uparrow\rangle$ is reaching 95.62%, which is considered a complete scenario. The intermediate states in this propagation are $|11\rangle$, $|18\rangle$, $|20\rangle$, $|25\rangle$, $|27\rangle$, $|28\rangle$, $|31\rangle$, $|35\rangle$, $|27\rangle$, $|38\rangle$, $|41\rangle$, $|43\rangle$, and $|45\rangle$. For the local spin-flip on Ni1, we directly choose the two sub-states $|11 \downarrow\rangle$ and $|13 \uparrow\rangle$ as initial and final states, respectively. The energy difference between the two states is 2.0×10^{-6} eV (see Table I). After a global optimization of the laser pulse with our genetic algorithm and the propagation with the optimized laser pulse, the spin-flip process from spin-down β to spin-up α on Ni1 atom is achieved with a fidelity of 94.60% [as shown in Fig. 7(b)]. The time-dependent population of the initial, final, and intermediate states is illustrated in Fig. 7(b). In this process, the intermediate states are $|5\rangle$, $|7\rangle$, $|10\rangle$, $|14\rangle$, $|16\rangle$, $|21\rangle$, $|25\rangle$, $|27\rangle$, $|28\rangle$, $|30\rangle$, $|31\rangle$, $|33\rangle$, $|40\rangle$, $|41\rangle$, $|48\rangle$, and $|50\rangle$. In addition, the optimized parameters of the laser pulse are θ = 319.50°, ϕ = 353.95°, FWHM = 396.45 fs, E_{laser} = 3.407 eV, and chirp = 1.005 (see Table II). The population between the initial state $|18 \downarrow\rangle$ (spin density is localized on Ni2 with $E_{|18\downarrow\rangle}$ = 779.883 meV; see Table I) and the final state $|20 \uparrow\rangle$ (spin density is localized on Ni2 with $E_{|20\uparrow\rangle}$ = 779.884 meV) via several intermediate states is also achieved and displayed in Fig. 7(c). The energy difference between the initial and final state is 10^{-6} eV, and the corresponding optimized laser parameters are shown in Table II.
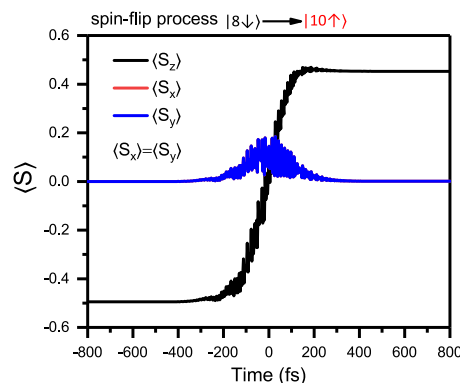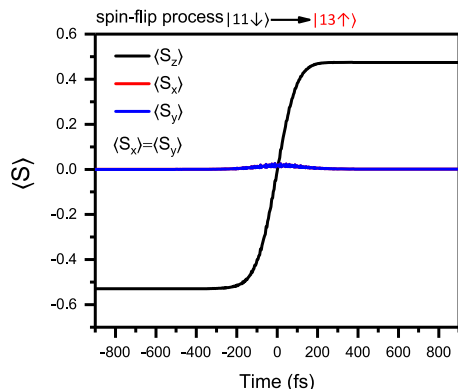

FIG. 3. Time-dependent expectation values of the spin components (spin-flip process $|8 \downarrow\rangle \rightarrow |10 \uparrow\rangle$). $\uparrow$ and $\downarrow$ denote the spin direction of the corresponding states.

The fidelity of this scenario reaches 79.62%, and the whole spin-flip process is accomplished within 201.24 fs. Herein, many intermediate states are accomplished, for instance, $|8\rangle$, $|23\rangle$, $|26\rangle$, $|29\rangle$, $|36\rangle$, $|39\rangle$, $|42\rangle$, $|46\rangle$, and $|49\rangle$. Another possible local spin-flip scenario on Ni1 is achieved by selecting $|21 \downarrow\rangle$ ($E_{|21\downarrow\rangle}$ = 782.012 meV) and $|23 \uparrow\rangle$ ($E_{|23\downarrow\rangle}$ = 782.013 meV) as initial and final states, which are two sub-states stemming from the same triplet state. The energy difference between the initial and final states is 1.0×10^{-6} eV. We show the time-dependent population of the initial (black dashed line), final (red solid line), and intermediate (solid lines in different colors) states in Fig. 7(d). The fidelity of this scenario is 94.78%, and the intermediate states are $|4\rangle$, $|8\rangle$, $|11\rangle$, $|18\rangle$, $|24\rangle$, $|25\rangle$, $|28\rangle$, $|31\rangle$, $|37\rangle$, $|38\rangle$, $|41\rangle$, $|44\rangle$, $|45\rangle$, $|48\rangle$, and $|52\rangle$. The corresponding optimized laser parameters are shown in Table II. Likewise, the local spin-flip process on Ni3 is accomplished by choosing $|5 \downarrow\rangle$ and $|7 \downarrow\rangle$ as initial and target states, respectively. $E_{|5\downarrow\rangle}$ and $E_{|7\uparrow\rangle}$ are 10.006 and 10.007 meV, respectively. The energy difference between them is 1.0×10^{-6} eV. The fidelity of this spin-down spin-up process is reaching 19.28%. Note that the time-dependent population of the initial, final, and intermediate states is not shown here. However, we show the optimized parameters of the laser pulse in Table II.

B. Spin-transfer scenarios

Additionally, the spin-transfer processes can also be accomplished using the EOM-CCSD method together with the Lambda process. The study of different spin-transfer processes denotes an essential topic in the development of spin-logic circuits.[111] A spin-transfer scenario happens when the spin of the initial and target states has the same direction but is localized on different atoms. According to the spin density distribution on Ni atoms, Ni1 → Ni2, Ni1 → Ni3, and Ni2 → Ni3 processes are achieved. Indeed, long-distance (around 27.14 Å) spin-transfer processes are accomplished between two magnetic centers through a carbon-based channel system [the C chains serve as long spin-transfer channels due to their p_z conjugated bonds; cf. Figs. 1(b) and 1(c)]. For example, in the process $|21 \downarrow\rangle \rightarrow |18 \downarrow\rangle$, we take states $|21 \downarrow\rangle$ (spin is localized on Ni1 with energy $E_{|21\rangle}$ = 782.012 meV) and $|18 \downarrow\rangle$ (spin is localized on

FIG. 4. Time-dependent expectation values of the spin components (spin-flip process $|11 \downarrow\rangle \rightarrow |13 \uparrow\rangle$). $\uparrow$ and $\downarrow$ denote the spin direction of the corresponding states (cf. Fig. 6).
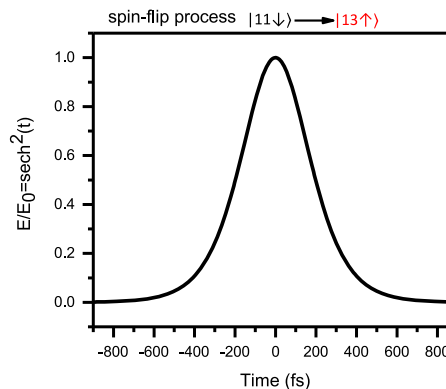
FIG. 6. Laser pulse envelope of field $\frac{E}{E_0} = \mathrm{sech}^2(t)$ for the local spin-flip process $|11 \downarrow\rangle \rightarrow |13 \uparrow\rangle$. $E_0 = 3.269 \times 10^{-3}$ a.u. (1.68×10^9 V/m) is the amplitude of the laser pulse used for this process (cf. Fig. 4).
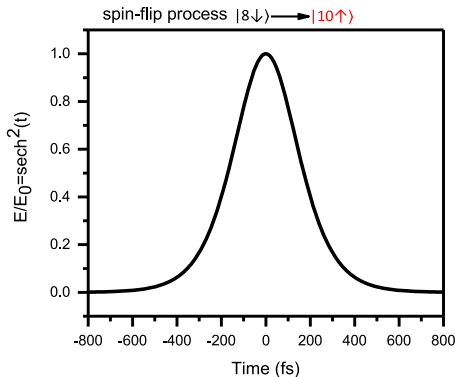
FIG. 5. Laser pulse envelope of field $\frac{E}{E_0} = \mathrm{sech}^2(t)$ for the local spin-flip process $|8 \downarrow\rangle \rightarrow |10 \uparrow\rangle$. $E_0 = 9.917 \times 10^{-3}$ a.u. (5.10×10^9 V/m) is the amplitude of the laser pulse used for this process.
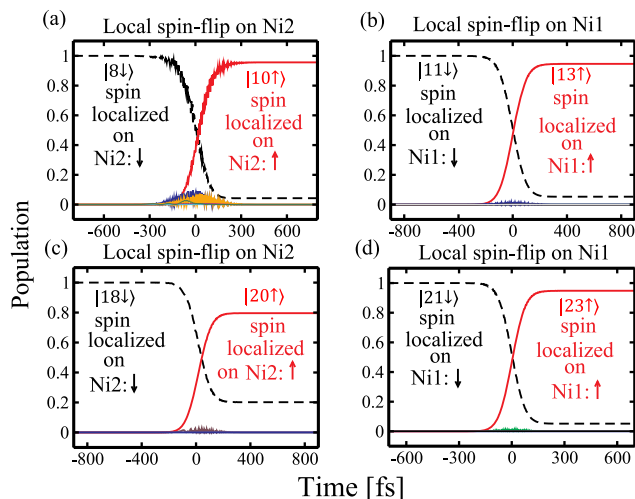
FIG. 7. Local spin-flip processes are accomplished on the Ni atoms: (a) $|8 \downarrow\rangle \rightarrow |10 \uparrow\rangle$ (spin is localized on Ni2). (b) $|11 \downarrow\rangle \rightarrow |13 \uparrow\rangle$ (spin is localized on Ni1). (c) $|18 \downarrow\rangle \rightarrow |20 \uparrow\rangle$ (spin is localized on Ni2). (d) $|21 \downarrow\rangle \rightarrow |23 \uparrow\rangle$ (spin is localized on Ni1). The time-dependent population of the initial, final, and intermediate states is represented by the black dashed line, red solid line, and solid lines in different colors, respectively. The two arrows $\downarrow$ and $\uparrow$ denote the spin direction of the corresponding states.

Ni2 with $E_{|18\downarrow\rangle} = 779.8823$ meV) as initial and target states, respectively. The corresponding time evolution of the population of each involved state is shown in Fig. 8(a). The fidelity of this spin-down spin-transfer process (Ni1 $\rightarrow$ Ni2) reaches 97.21%. It takes around 314.54 fs to accomplish the whole spin-transfer process. The dominant intermediate states are $|8\rangle$ (violet line in the upper panel) and $|11\rangle$ (blue line in the upper panel). We present the optimized parameters of the laser pulses in Table II. For instance, in this scenario $|21 \downarrow\rangle \rightarrow |18 \downarrow\rangle$, the optimized parameters of the laser pulse are $\theta = 225.71°$, $\phi = 279.67°$, $\gamma = 311.17°$, $\beta = 254.57°$, FWHM = 314.54 fs, $E_{laser} = 1.510$ eV, and a chirp of 1.002. In addition, by choosing the states $|11\rangle$ (initial) and $|18\rangle$ (target), a spin-down spin-transfer process (Ni1 $\rightarrow$ Ni2) is accomplished with a fidelity of 70.27% (see the Appendix). The spin density can also be moved from Ni1 to Ni2 under a single laser pulse by selecting $|11 \downarrow\rangle$ and $|8 \downarrow\rangle$ as initial and final states, respectively. The fidelity of this process and the corresponding optimized parameters of the laser pulse are shown in

the Appendix (see Table IV). In addition, the spin density can be transferred from the magnetic center Ni1 to Ni3. Herein, we take states $|13 \downarrow\rangle$ ($E_{|13\downarrow\rangle} = 12.816$ meV) and $|16 \downarrow\rangle$ ($E_{|16\downarrow\rangle} = 14.896$ meV). This scenario is also called a spin-down spin-transfer process. The energy difference between the above states ($|13 \downarrow\rangle$ and $|16 \downarrow\rangle$) is 2.08 meV. The difference is small enough to extend the lifetime of the energetically higher state by blocking the direct relaxation mechanisms while also being adequate to differentiate the two states for

TABLE II. Spin localized, possible scenarios and the parameters of the laser pulses are optimized with our genetic algorithm program and EOM-CCSD method: ΔE, the energy difference between the initial and last (target) states; the angles of incidence in spherical coordinates θ (°) and ϕ (°); the angle between the polarization of light and the optical plane γ (°); β (°), the ellipticity; the full width at half-maximum of the laser pulse (FWHM); the laser energy E_{laser}; the amplitude of the laser pulse; and the chirp, which indicates the linear sweep of the frequency with respect to the peak frequency. The ranges of θ (°) and ϕ (°) are from [0°, 180°] to [0°, 360°], respectively. In addition, the range of γ is [0°, 360°]. All the calculations are performed with the EOM-CCSD method.

Scenario	Spin localized	Process	Fidelity (%)	ΔE (eV)	θ (°)	ϕ (°)	γ (°)	β (°)	FWHM (fs)	E_{laser} (eV)	Chirp
Local spin–flip	Ni2	$\lvert 8\downarrow\rangle \rightarrow \lvert 10\uparrow\rangle$	95.62	2.0×10^{-6}	75.59	165.87	76.37	106.95	342.87	3.328	0.990
Local spin–flip	Ni1	$\lvert 11\downarrow\rangle \rightarrow \lvert 13\uparrow\rangle$	94.60	2.0×10^{-6}	319.50	353.95	44.92	221.04	396.45	3.407	1.001
Local spin–flip	Ni2	$\lvert 18\downarrow\rangle \rightarrow \lvert 20\uparrow\rangle$	79.62	1.0×10^{-6}	179.47	56.00	201.24	190.52	361.00	2.129	0.950
Local spin–flip	Ni1	$\lvert 21\downarrow\rangle \rightarrow \lvert 23\uparrow\rangle$	94.78	1.0×10^{-6}	341.48	292.28	350.89	129.10	309.84	2.231	0.997
Local spin–flip	Ni3	$\lvert 5\downarrow\rangle \rightarrow \lvert 7\uparrow\rangle$	19.28	1.0×10^{-6}	162.97	300.98	351.39	130.14	254.59	2.490	1.005
Spin-transfer	Ni1 → Ni2	$\lvert 21\downarrow\rangle \rightarrow \lvert 18\downarrow\rangle$	97.21	2.129×10^{-3}	225.71	279.67	311.17	254.57	314.54	1.510	1.002
Spin-transfer	Ni1 → Ni3	$\lvert 13\downarrow\rangle \rightarrow \lvert 16\downarrow\rangle$	82.10	2.080×10^{-3}	295.26	229.79	21.69	7.07	388.68	2.778	1.002
Spin-transfer	Ni2 → Ni3	$\lvert 8\downarrow\rangle \rightarrow \lvert 14\downarrow\rangle$	72.15	3.789×10^{-3}	136.38	181.65	156.74	185.58	314.24	3.167	1.006
Spin-transfer	Ni2 → Ni1	$\lvert 8\downarrow\rangle \rightarrow \lvert 11\downarrow\rangle$	84.34	1.708×10^{-3}	59.05	113.13	157.12	331.97	69.37	2.238	1.035

an external laser pulse. The corresponding time-dependent population of each involved state is shown in Fig. 8(b). We find a fidelity of 82.10%. The main intermediate states are $\lvert 7\rangle$ and $\lvert 43\rangle$, and we see a few Rabi oscillations (clear-cut) that mean an ultrafast transfer scenario within 388.68 fs. Among the optimized parameters of the laser pulse are $\theta = 295.26°$, $\phi = 229.79°$, $\gamma = 21.69°$, and $E_{laser} = 2.778$ eV. Since we have three magnetic centers (Ni1, Ni2, and Ni3), also spin transfer scenarios can be achieved to move the spin density from Ni2 to Ni3 along the carbon atoms. Here, we present the Λ process scenario $\lvert 8\downarrow\rangle$ (initial state) to $\lvert 14\downarrow\rangle$ (target state), which is one among these scenarios. At the many-body state $\lvert 8\downarrow\rangle$, the spin density is localized on Ni2 with the energy of $E_{\lvert 8\downarrow\rangle} = 11.106$ meV. In $\lvert 14\downarrow\rangle$, the spin density is localized on Ni3 with the energy of $E_{\lvert 14\downarrow\rangle} = 14.895$ meV. We give the corresponding time-evolution of the population of each involved state in Fig. 8(c) and the optimized parameters of the laser pulse in Table II. The fidelity of this process is 72.15%, and the intermediate states are $\lvert 5\rangle$, $\lvert 7\rangle$, $\lvert 10\rangle$, $\lvert 11\rangle$, $\lvert 13\rangle$, $\lvert 16\rangle$, $\lvert 18\rangle$, $\lvert 20\rangle$, $\lvert 25\rangle$, $\lvert 27\rangle$, $\lvert 28\rangle$, $\lvert 30\rangle$, $\lvert 31\rangle$, $\lvert 33\rangle$, $\lvert 37\rangle$, $\lvert 40\rangle$, $\lvert 41\rangle$, $\lvert 43\rangle$, and $\lvert 50\rangle$. The spin density can be moved from Ni2 to Ni1 (Ni2 → Ni1) with a single laser pulse by choosing $\lvert 8\downarrow\rangle$ and $\lvert 11\downarrow\rangle$ as initial and target states, respectively. The energy difference between them is 1.708 meV (see Table II), which is large enough to render the two states distinguishable for an external laser pulse and small enough to suppress the direct relaxation processes. Figure 8(d) illustrates the time evolution of the population of each involved state (initial, final, and intermediate states). The fidelity of this reversed spin-down spin-transfer process ($\lvert 8\downarrow\rangle \rightarrow \lvert 11\downarrow\rangle$) with a different laser pulse and the corresponding optimized parameters of the laser pulse is shown in Table II as well. Moreover, another spin-down spin-transfer process $\lvert 18\downarrow\rangle \rightarrow \lvert 5\downarrow\rangle$ (Ni2 → Ni1) is achieved with a fidelity of 69.02% (see the Appendix). Furthermore, the spin density can be moved from Ni3 to Ni1 or from Ni3 to Ni2 under a single laser pulse. In this way, several spin-down spin-transfer processes are accomplished. We show the optimized parameters of the laser pulse together with the time-dependent population of each involved state in the Appendix.
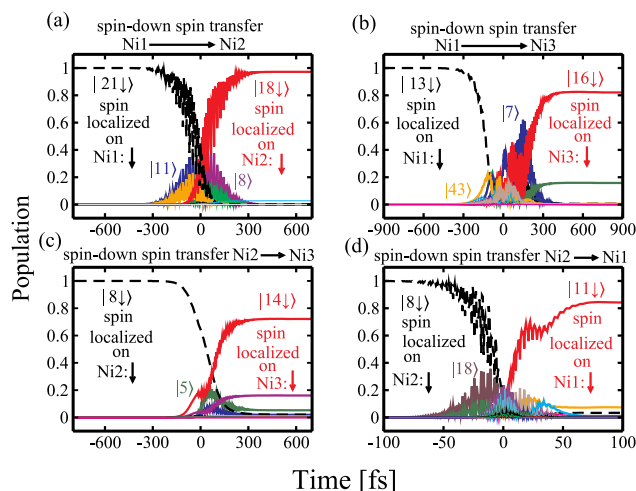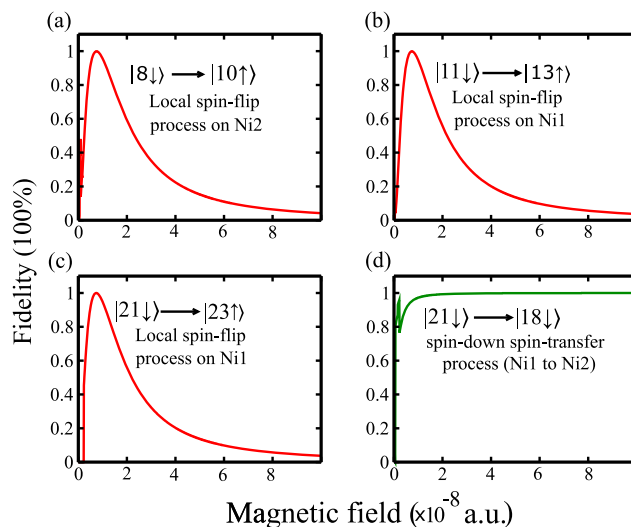

FIG. 8. Global spin-down spin-transfer processes are accomplished between the magnetic centers along the carbon atoms: (a) $\lvert 21\downarrow\rangle \rightarrow \lvert 18\downarrow\rangle$ (Ni1 → Ni2). (b) $\lvert 11\downarrow\rangle \rightarrow \lvert 13\downarrow\rangle$ (Ni1 → Ni3). (c) $\lvert 18\downarrow\rangle \rightarrow \lvert 20\downarrow\rangle$ (Ni2 → Ni3). (d) $\lvert 21\downarrow\rangle \rightarrow \lvert 23\downarrow\rangle$ (Ni2 → Ni1). The time-dependent population of the initial, final, and intermediate states is represented by the black dashed line, red solid line, and solid lines in different colors, respectively. The two arrows ↓ and ↑ denote the spin direction of the corresponding states.

C. Effect of an inhomogeneous magnetic field and impact of the direction of the single laser on the spin-dynamics processes

Since the fidelity of the laser-driven ultrafast spin dynamics can be affected by the magnetic field strength, in this subsection, we study the influence of the magnetic field[112–116] on the spin-dynamic processes (we take as an example three spin-flip and one spin-transfer scenario). We maintain the magnetic field angles ($\theta = 0.00°$

and $\phi = 0.00°$) and vary the strength of the magnetic field from 0 to 1.0×10^{-8} a.u. Figures 9(a)–9(c) show the effect of an inhomogeneous magnetic field on the local spin-flip processes on Ni2 and Ni1, respectively. In the case of the local spin-flip process on Ni2 $|8 \downarrow\rangle \rightarrow |10 \uparrow\rangle$ (where the spin is localized on Ni2 on both states), the fidelity increases within a small magnetic field ranging from 0 to 1.0×10^{-8} a.u. [as displayed in Fig. 9(a)]. At the same range of the magnetic field, the fidelity of the local spin-down spin-up flip process on Ni1 $|11 \downarrow\rangle \rightarrow |13 \uparrow\rangle$ (spin is localized on Ni1 for both states) is gradually increasing to reach its limit [see Fig. 9(b)]. This is explained by the fact that when the magnetic field increases, the Zeeman splitting tends to get stronger, making each state more individually addressable. Moreover, this increase is also corroborated by the effect of the magnetic field on the local spin-flip scenario on Ni1 $|21 \downarrow\rangle \rightarrow |23 \uparrow\rangle$. Again, we see that the fidelity increases and reaches its limit at 1.0×10^{-8} a.u. [as shown in Fig. 9(c)]. Note that the parameters of the laser pulse are optimized at this magnetic field strength. When $B = 0.00$ a.u., the fidelity is 0.00%, which means that the α and β states are indistinguishable. For the three local spin-flip processes, when the magnetic field strength exceeds 1.0×10^{-8} a.u., the fidelity begins to slowly decrease. This is attributed to the modification in the spin-mixed intermediate states included in the spin-flip process. The spin-mixed intermediate states tend to become spin pure as the magnetic field is stronger, which in turn blocks the channels and inhibits the spin-flip process. As the magnetic field gets stronger, the SOC becomes comparably weak (Paschen–Back effect). In those processes, we keep all the intermediate states, which play the most significant role and can be strongly affected by the power of the magnetic field. Note also that the level crossing, which is caused by a stronger magnetic field, can modify the state ordering and phase elements of the excited intermediate states.[44] For the spin-down spin-transfer process $|21 \downarrow\rangle \rightarrow |18 \downarrow\rangle$ (Ni1 → Ni2), the fidelity also increases rapidly with the magnetic field strength ranging from 0 to 1.98×10^{-9} a.u. and reaches 95.93% [as illustrated in Fig. 9(d)]. Then, the fidelity begins to decrease sharply (because there is an avoided level crossing between the intermediate states) until reaching 77.23% with a magnetic field value of 2.39×10^{-9} a.u. However, when $B > 2.39 \times 10^{-9}$ a.u., the fidelity returns to increase until it reaches its limit with $B = 1 \times 10^{-8}$ a.u. The reason for this scenario is the same as in the case of the spin-flip process: The spin-mixed states become spin-pure states. When $B \geq 1.0 \times 10^{-8}$ a.u., the spin-down spin-transfer process $|21 \downarrow\rangle \rightarrow |18 \downarrow\rangle$ is preserved because the intermediate states are predominantly pure spin states, which can be barely changed by increasing the magnetic field strength. This offers the addressability of the local logic-circuit on a magnetic center (Ni1, Ni2, and Ni3) and the high precision of information interchange between these magnetic centers along the carbon atoms. Next, we investigate the effect of the direction of the single laser pulse by varying their angles on the spin-dynamics processes. Here, the impact of θ and ϕ, which are described as the polar and azimuthal angles in spherical coordinates, respectively, on the local spin-flip process on Ni2 $|8 \downarrow\rangle \rightarrow |10 \uparrow\rangle$ and spin-down spin-transfer $|21 \downarrow\rangle \rightarrow |18 \downarrow\rangle$ is studied here. It should be noted that the range of θ is from 0° to 180° (180°–360° is the reflection of the original panel) and ϕ from 0° to 360°. Furthermore, the magnetic field value is selected to 1.0×10^{-8} a.u., and the parameters of the optimized laser pulses are also listed (excluding θ and ϕ). We plot the effect of θ and ϕ of the laser pulse on the spin-flip process fidelity in Fig. 10. We see four small

FIG. 9. The effect of an inhomogeneous magnetic field on the spin-dynamics processes: (a) Local spin-flip on Ni2 ($|8 \downarrow\rangle \rightarrow |10 \uparrow\rangle$). (b) Local spin-flip on Ni1 ($|11 \downarrow\rangle \rightarrow |13 \uparrow\rangle$). (c) Local spin-flip on Ni1 ($|21 \downarrow\rangle \rightarrow |23 \uparrow\rangle$). (d) Spin-down spin-transfer process ($|21 \downarrow\rangle \rightarrow |18 \downarrow\rangle$) (Ni1 → Ni2). The 0% fidelity at around B = 0 a.u. is simply due to the fact that α and β states are indistinguishable at this magnetic field.

regions with higher fidelity (94.50%). We find that a little change of θ and ϕ can decrease this fidelity. Figure 11 shows the effect of those angles on the spin-transfer process $|21 \downarrow\rangle \rightarrow |18 \downarrow\rangle$. We obtain some areas that include higher fidelity (more than 92.30%). For instance, a higher fidelity value is appearing when $\theta_1° \in [0°, 18°]$ and $\theta_2° \in [0°, 18°]$ together with $\phi_1 \in [104°, 105°]$ and $\phi_2 \in [104°, 109°]$. When $\theta = 163.03°$ and $\phi = 252.48°$, we see a higher fidelity, indicating a spin-transfer between Ni1 and Ni2. A noticeable point is due to the laser pulses being elliptically polarized. Thus, when θ is equivalent to 0°, the fidelity has a twofold symmetry with respect to the azimuthal angle ϕ (ranging from 0.756 to 0.947), in particular for the spin-flip process $|21 \downarrow\rangle \rightarrow |18 \downarrow\rangle$.

## D. Impact of the double laser pulse on the spin-flip scenarios

Additionally, we investigate the double-laser[117–119] pulse-induced spin dynamic processes. We apply a second pulse, which is specified by the following formula, to control the process efficiency:

$$\frac{\partial c_n(t)}{\partial t} = \frac{-i}{\hbar} \sum_k \langle \Phi_n | \hat{H}_{\text{int1}}(t) + \hat{H}_{\text{int2}}(t + \delta t) | \Phi_k \rangle c_k(t)$$
$$\times \exp\left(-i(E_k - E_n)t/\hbar\right). \quad (4)$$

$\hat{H}_{\text{int1}}(t)$ and $\hat{H}_{\text{int2}}(t)$ describe the interaction Hamiltonians of the initial and final laser pulses. δt is the time delay between two successive laser pulses (2× FWHM is used here, i.e., the time delay between the two pulse maxima is set to double the full width at half maximum). The spin-flip process on Ni2 $|8 \downarrow\rangle \rightarrow |10 \uparrow\rangle$ and the spin-down spin-transfer process $|21 \downarrow\rangle \rightarrow |18 \downarrow\rangle$ (spin density is moved from Ni1 → Ni2) are performed under double laser-pulses. In this
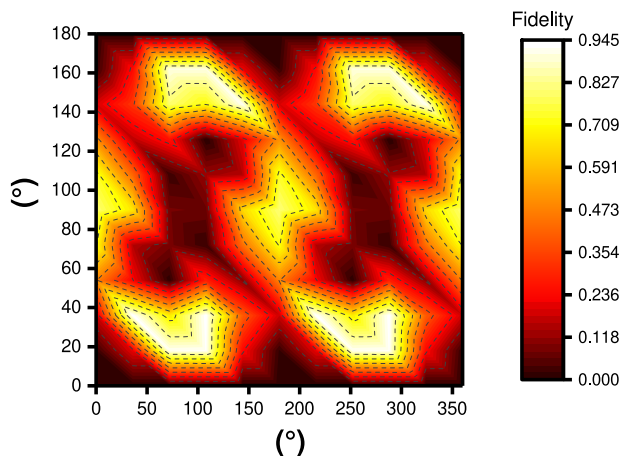
FIG. 10. The influence of the polar angle $\theta°$ and the azimuthal angle $\phi°$ of the laser pulse on the $|8\downarrow\rangle \rightarrow |10\uparrow\rangle$ ultrafast local spin-flip process on Ni2 by varying them within a full angle range $[0°, 360°]$. Note that the laser pulse is elliptically polarized. Thus, the extended part of $\theta \in [180°, 360°]$ is the reflection of the original panel.
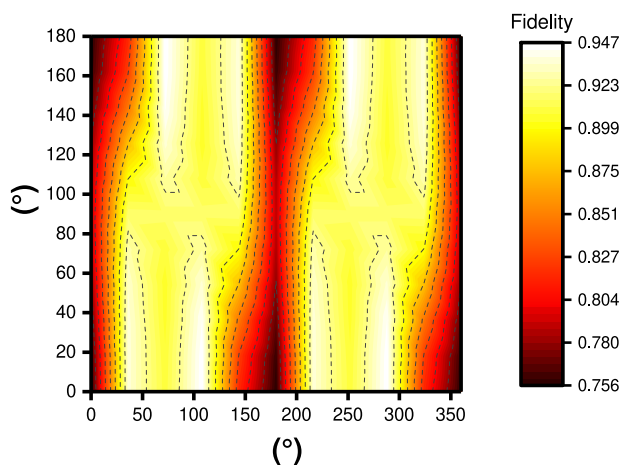

FIG. 11. The influence of the polar angle $\theta°$ and the azimuthal angle $\phi°$ of the laser pulse on the $|21\downarrow\rangle \rightarrow |18\downarrow\rangle$ ultrafast spin-transfer process on the Ni$_3$@C$_{63}$H$_{54}$ molecule.

situation, the magnetic field is still applied with B = 1.0×10^{-8} a.u., $\theta = 0.00°$, and $\phi = 0.00°$. As done with a single laser pulse, in the local spin-flip process $|8\downarrow\rangle \rightarrow |10\uparrow\rangle$ on Ni2, we take $|8\downarrow\rangle$ and $|10\uparrow\rangle$ as initial and final states, respectively. We show their corresponding time evolution of the population of each active state in Fig. 12. By using the modified genetic algorithm and after several generations, the double laser pulses successfully induce the fidelity of this process (95.65%). Herein, the optimized parameters of the laser pulse are $\theta = 334.27°$, $\phi = 23.82°$, $\gamma = 345.46°$, $\beta = 120.77°$, FWHM = 383.52, and chirp = 1.010. In addition, under successive double laser pulses,
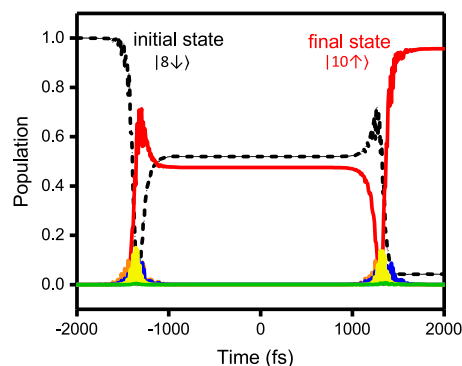
FIG. 12. The double laser-pulse-induced spin-flip ($|8\downarrow\rangle$ to $|10\uparrow\rangle$) processes on Ni3 and Ni2, respectively. Time evolution of the population of the initial, intermediate, and final states with a delay between the two pulses of $2 \times$ FWHM.
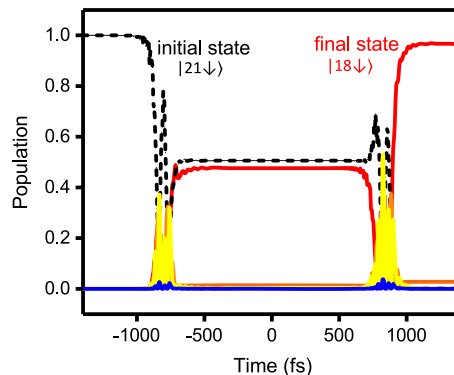
FIG. 13. The double laser-pulse-induced spin-transfer ($|21\downarrow\rangle$ to $|18\downarrow\rangle$) processes on Ni3 and Ni2, respectively. Time evolution of the population of the initial, intermediate, and final states with a delay between the two pulses of $2 \times$ FWHM.

the spin density can be moved between the magnetic centers Ni1 and Ni2. For example, we take the states $|21\downarrow\rangle$ (initial) and $|18\downarrow\rangle$ (target) to transfer the spin from Ni1 $\rightarrow$ Ni2. The fidelity of this process is reaching 96.63%. Therefore, we can say that the double laser pulses successfully induce the spin-down spin-transfer process $|21\rangle\downarrow \rightarrow |18\downarrow\rangle$. The time evolution of the population of each involved state is illustrated in Fig. 13. Among the main intermediate states in this scenario, we predominately find $|5\rangle$, $|7\rangle$, $|8\rangle$, $|10\rangle$, $|14\rangle$, $|30\rangle$, $|31\rangle$, and $|50\rangle$. In addition, the optimized parameters of the laser pulse are $\theta = 254.13°$, $\phi = 34.71°$, $\gamma = 45.75°$, $\beta = 331.02°$, FWHM = 235.12 fs, and chirp = 0.989.

V. CONCLUSION

In summary, EOM-CCSD calculations, Mulliken population analysis, under a spin–orbital coupling, and a static magnetic field reveal that the spin density is unequally distributed on the Ni atoms.

29 April 2024 13:08:03

TABLE III. Spin density, energies, and expectation values of the spin angular momentum components for the spin-flip and spin-transfer scenarios on $Ni_3@C_{63}H_{54}$ for the appropriate many-body states (some states) before and after the inclusion of spin–orbit coupling and the magnetic field. The sign of $\langle S_x \rangle$, $\langle S_y \rangle$, and $\langle S_z \rangle$ signifies the spin direction: the positive and negative values are spin-up $\alpha \uparrow$ and spin-down $\beta \downarrow$, respectively.

Method	States	Spin density before SOC and B			Energy, spin directions, and spin density after SOC and B						
		Ni1	Ni2	Ni3	E (meV)	$\langle S_x \rangle$	$\langle S_y \rangle$	$\langle S_z \rangle$	Ni1	Ni2	Ni3
EOM-CCSD	$|52\rangle$	0.000	1.044	0.000	3564.072	0.0000	0.0000	0.0000	0.000	0.000	0.000
	$|51\rangle$	0.000	0.000	0.000	3558.288	0.0000	0.0000	0.0000	0.000	0.000	0.000
	$|50\rangle$	0.000	−1.044	0.000	3486.300	−0.0001	0.0000	0.9938	0.014	0.029	0.021
	$|49\rangle$	1.041	0.000	0.000	3486.295	0.0001	0.0001	0.0000	0.000	0.000	0.000
	$|48\rangle$	0.000	0.000	0.000	3486.294	−0.0001	0.0000	−0.9938	−0.014	−0.029	−0.021
	$|47\rangle$	−1.041	0.000	0.000	3475.897	0.0000	0.0000	0.9999	0.011	0.019	0.042
	$|46\rangle$	0.000	0.000	0.000	3475.897	0.0000	−0.0001	0.0000	0.000	0.000	0.000
	$|45\rangle$	0.000	0.000	0.000	3475.896	0.0000	0.0000	−0.9999	−0.011	−0.019	−0.042
	$|44\rangle$	0.000	0.000	1.054	2996.546	0.0000	0.0000	0.0000	0.000	0.000	0.000
	$|43\rangle$	0.000	0.000	0.000	2913.604	0.0000	0.0000	0.8691	0.213	0.126	0.295
	$|41\rangle$	0.000	0.000	0.000	2913.603	0.0000	0.0001	−0.8691	−0.213	−0.126	−0.295
	$|40\rangle$	0.000	0.000	0.000	2906.161	0.0001	0.0001	0.9572	0.264	0.383	0.068
	$|39\rangle$	0.000	0.000	0.000	2906.160	−0.0001	−0.0001	0.0000	0.000	0.000	0.000
	$|38\rangle$	0.000	0.000	1.064	2906.159	0.0000	0.0000	−0.9572	−0.264	−0.383	−0.068
	$|36\rangle$	0.000	0.000	−1.064	2887.498	−0.0001	−0.0001	0.0000	0.000	0.000	0.000
	$|34\rangle$	0.000	0.000	0.000	2753.049	0.0000	0.0000	0.0000	0.000	0.000	0.000
	$|32\rangle$	1.055	0.000	0.000	2556.113	0.0000	0.0000	0.0000	0.000	0.000	0.000
	$|30\rangle$	−1.055	0.000	0.000	2509.923	0.0000	0.0000	0.9921	0.047	0.063	0.015
	$|26\rangle$	−0.245	−0.144	−0.339	2508.236	0.0000	0.0000	0.0000	0.000	0.000	0.000
	$|24\rangle$	0.000	0.000	0.000	1239.732	0.0000	0.0000	0.0000	0.000	0.000	0.000
	$|22\rangle$	0.000	0.000	0.000	782.013	0.0000	0.0000	0.0000	0.000	0.000	0.000
	$|20\rangle$	0.294	0.301	0.179	779.884	0.0000	0.0000	0.9985	0.000	1.042	0.000
	$|19\rangle$	0.000	0.000	0.000	779.883	−0.0001	0.0000	0.0000	0.000	0.000	0.000
	$|17\rangle$	0.014	0.030	0.021	19.174	0.0000	0.0000	0.0000	0.000	0.000	0.000
	$|15\rangle$	−0.014	−0.030	−0.021	14.895	−0.0003	0.0001	0.0000	0.000	0.000	0.000
	$|12\rangle$	−0.011	−0.019	−0.042	12.814	0.0000	−0.0002	0.0000	0.000	0.000	0.000
	$|9\rangle$	0.000	0.000	0.000	11.106	0.0005	0.0005	0.0000	0.000	0.000	0.000
	$|1\rangle$	0.000	0.000	0.000	0.000	0.0000	0.0000	0.0000	0.000	0.000	0.000

Therefore, local spin-flip scenarios on Ni1 (Ni2 or Ni3) are accomplished on a closed system of three carbon chains to which three nickel atoms are attached ($Ni_3@C_{63}H_{54}$) via Λ processes. Furthermore, according to the spin density distribution, three possible long-distance spin-transfer processes Ni1 → Ni2 (Ni2 → Ni1), Ni1 → Ni3 (Ni3 → Ni1), and Ni2 → Ni3 (Ni3 → Ni1) are achieved. The best fidelity of 97.21% is reached for the $|21 \downarrow\rangle$ (spin density is localized on Ni1) → $|18 \downarrow\rangle$ (spin density is localized on Ni2) spin-transfer scenario. The effect of the magnetic field on three local spin-flip scenarios and one spin-down spin-transfer scenario is calculated. Herein, we find that the spin-transfer process is preserved, while the local spin-flip processes on Ni atoms can be suppressed under different magnetic field strengths. We show that with a small re-orientation of the laser pulse, the fidelity is dramatically changed. The double laser pulse successfully induces the spin-flip and spin-transfer processes. We believe that our system is a favorable candidate for devices for next-generation spin logic applications due to the advanced spin density localization that enables coherent spin manipulation.

AUTHOR DECLARATIONS

Conflict of Interest

The authors have no conflicts to disclose.

Author Contributions

Mohamed Barhoumi: Conceptualization (equal); Data curation (equal); Formal analysis (equal); Investigation (equal); Methodology (equal); Writing – original draft (equal); Writing – review & editing (equal). **Jing Liu**: Data curation (equal); Formal analysis (equal); Investigation (equal); Methodology (equal). **Georgios Lefkidis**: Investigation (equal); Resources (equal); Supervision (equal); Writ-

29 April 2024 13:08:03
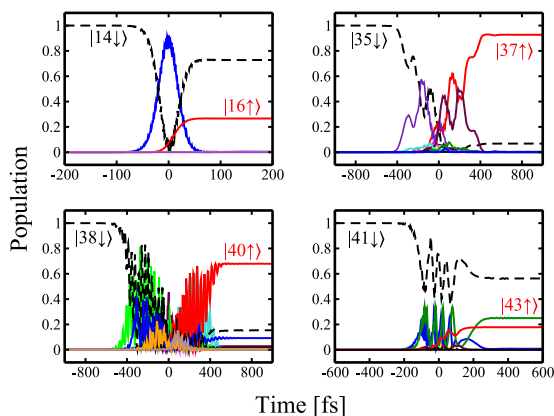
FIG. 14. Different spin-flip processes are achieved: a local spin-flip on Ni3 ($|14\rangle \rightarrow |16\rangle$); a simultaneous spin-flip on Ni1, Ni2, and Ni3 ($|35\rangle \rightarrow |37\rangle$); a simultaneous spin-flip on Ni1 and Ni2 ($|38\rangle \rightarrow |40\rangle$); and a simultaneous spin-flip on Ni1, Ni2, and Ni3 ($|41\rangle \rightarrow |43\rangle$). Note the time-dependent population of the initial (black dashed line), final or target (red solid line), and intermediate (solid lines in different colors) states.

ing – review & editing (equal). **Wolfgang Hübner**: Investigation (equal); Resources (equal); Supervision (equal); Writing – review & editing (equal).

DATA AVAILABILITY

The data that support the findings of this study are available from the corresponding author upon reasonable request.

APPENDIX: THEORY, SPIN-DENSITY DISTRIBUTION, AND SPIN DYNAMICS PROCESSES

1. Quantum-theory method

Before EOM-CCSD, we use the coupled-cluster (CC)[85,86] method, which is among the most precise *ab initio* quantum chemical computation techniques for determining the correlation energy of many-electron systems.[120–126] It uses the exponential cluster operator to build the many-body wave functions from the molecular orbitals received by employing the Hartree–Fock approach. The next ansatz describes the wave function of the CC concept,

$$|\Psi\rangle = e^{\hat{T}}|\Phi_0\rangle. \tag{A1}$$

$|\Phi_0\rangle$ is the ground state wave function acquired from the Hartree–Fock method, which is the reference state of the CC calculations. $\hat{T}$ is the cluster operator. When $\hat{T}$ acts on the reference determinant $|\Phi_0\rangle$, a complete set of excited Slater determinants can be produced. The operator $\hat{T}$ form can be represented as

$$\hat{T} = \hat{T}_1 + \hat{T}_2 + \hat{T}_3 + \cdots \hat{T}_N. \tag{A2}$$

$\hat{T}_1$, $\hat{T}_2$, and $\hat{T}_3$ collectively designate single, double, and triple excitation operators, respectively. These operators can be written in second quantization, e.g., $\hat{T}_1$ and $\hat{T}_2$ are

$$\hat{T}_1 = \sum_a \sum_r t_a^r \hat{a}_r^+ \hat{a}_a, \tag{A3}$$

$$\hat{T}_2 = \frac{1}{4} \sum_{a,b} \sum_{r,s} t_{ab}^{rs} \hat{a}_r^+ \hat{a}_s^+ \hat{a}_b \hat{a}_a. \tag{A4}$$

t_a^r and t_{ab}^{rs} are the expansion coefficients of the corresponding operators and are called amplitudes. The subscripts a, b and the superscripts r and s denote the index of occupied and unoccupied orbitals, respectively. $\hat{a}^+$ and $\hat{a}$ are creation and annihilation operators, respectively. In the second quantization, the creation operator is defined as $\hat{a}_a^+|1,2,\ldots,N\rangle = |a,1,2;\ldots,N\rangle$, while its adjoint is the corresponding annihilation operator $\hat{a}_a|a,1,2,\ldots,N\rangle = |1,2,\ldots,N\rangle$. Expanding the exponential $e^{\hat{T}}$ function as a Taylor series, we get an infinite series

$$e^{\hat{T}} = 1 + \hat{T}_1 + \hat{T}_2 + \frac{1}{2}\hat{T}_1^2 + \frac{1}{2}\hat{T}_1\hat{T}_2 + \frac{1}{2}\hat{T}_2\hat{T}_1 + \frac{1}{2}\hat{T}_2^2 + \cdots. \tag{A5}$$

Unfortunately, the CC equations can only be used to compute the ground wave function of a molecular system. We employ the EOM-CCSD method to compute the excited state wave functions. An excited EOM-CCSD state can be provided by

$$|\Phi^{\text{EOM-CCSD}}\rangle = \hat{R}|\Phi^{\text{CCSD}}\rangle. \tag{A6}$$

$\hat{R} = \hat{R}_1 + \hat{R}_2$ is the excitation operator, which is cut behind single and double excitations.

2. Spin density distribution and spin dynamics processes

Here, we give the spin density distribution, energies, and expectation values of the spin angular momentum elements for the spin-flip and spin-transfer scenarios on our structure for the appropriate many-body states (some states) before and after the inclusion of spin–orbit coupling and the magnetic field in Table III. In addition, other spin-flip scenarios are accomplished. We present some of them in Fig. 14. For instance, a simultaneous spin-flip process on the Ni1 and Ni2 atoms is also achieved. Herein, the states $|38\downarrow\rangle$ and $|40\uparrow\rangle$ are selected as initial and final states, respectively. The fidelity of this process reaches 67.93%, which indicates that a successful scenario is accomplished. The time evolution of the population of each involved state is shown in Fig. 14. The optimized parameters of the laser pulse are $\theta = 240.28°$, $\phi = 300.68°$, $\gamma = 67.53°$, FWHM = 404.75 fs, and chirp = 0.999 (see Table IV for more details). Two other possible Λ spin-flip processes simultaneously on the Ni1, Ni2, and Ni3 atoms are accomplished. They are $|35\rangle \rightarrow |37\rangle$ and $|41\rangle \rightarrow |43\rangle$. The time evolution of the population of each involved state is shown in Fig. 14. We find that the fidelity of the process $|35\rangle \rightarrow |37\rangle$ reaches 92.71%, which is considered a complete process, while it is 17.79% for the process $|41\rangle \rightarrow |43\rangle$. The optimized parameters of the laser pulses are depicted in Table IV. In addition, we take $|14\rangle$ and $|16\rangle$ as initial and target states, respectively. The spin density is localized on Ni3 for both states. It is a local spin-flip on the Ni3 atom. The fidelity of this process is reaching 26.60%. The optimized parameters of the laser pulse are shown in Table IV. Note that the lower fidelity obtained for the processes $|14\rangle \rightarrow |16\rangle$ and $|41\rangle \rightarrow |43\rangle$ can be improved when a small magnetic field ($< 1 \times 10^{-8}$ a.u.) is used. However, the spin-density localization becomes very weak, and therefore, it does

TABLE IV. Spin localized, possible scenarios where the parameters of the laser pulses are optimized with our genetic algorithm program and EOM-CCSD method: ΔE, the energy difference between the initial and final states; the angles of incidence in spherical coordinates θ (°) and ϕ (°); the angle between the polarization of light and the optical plane, γ (°); β (°), the ellipticity; the full width at half-maximum of the laser pulse (FWHM); the laser energy E_{laser}; the amplitude of the laser pulse; and the chirp, which indicates the linear sweep of the frequency with respect to the peak frequency. The ranges of θ (°) and ϕ (°) are from [0°, 180°] to [0°, 360°], respectively. In addition, the range of γ is [0°, 360°]. All the calculations are performed with the EOM-CCSD method.

Scenario	Spin localized	Process	Fidelity (%)	ΔE (eV)	θ (°)	ϕ (°)	γ (°)	β (°)	FWHM (fs)	E_{laser} (eV)	Chirp
Local spin–flip	Ni3	$\lvert 14\downarrow\rangle \to \lvert 16\uparrow\rangle$	26.60	1.00×10^{-6}	296.66	297.46	230.36	161.31	103.34	2.360	0.992
Spin–flip	Ni1 and Ni2 and Ni3	$\lvert 35\downarrow\rangle \to \lvert 37\uparrow\rangle$	92.71	1.00×10^{-6}	235.25	155.10	165.02	292.46	461.56	2.699	1.000
Spin–flip	Ni1 and Ni2	$\lvert 38\downarrow\rangle \to \lvert 40\uparrow\rangle$	67.93	2.00×10^{-6}	240.28	300.68	67.53	229.46	404.75	0.891	0.999
Spin–flip	Ni1 and Ni2 and Ni3	$\lvert 41\downarrow\rangle \to \lvert 43\uparrow\rangle$	17.79	1.00×10^{-6}	171.30	240.83	186.74	35.83	270.57	3.236	0.977
Spin-transfer	Ni3 $\to$ Ni2	$\lvert 5\downarrow\rangle \to \lvert 8\downarrow\rangle$	63.29	1.10×10^{-3}	63.34	271.25	355.81	135.20	494.31	2.524	0.992
Spin-transfer	Ni3 $\to$ Ni1	$\lvert 5\downarrow\rangle \to \lvert 11\downarrow\rangle$	60.21	2.808×10^{-3}	234.95	334.21	283.72	255.71	476.98	2.866	0.987
Spin-transfer	Ni3 $\to$ Ni2	$\lvert 5\downarrow\rangle \to \lvert 18\downarrow\rangle$	54.23	769.877×10^{-3}	55.67	197.22	114.70	8.79	474.26	0.037	0.985
Spin-transfer	Ni3 $\to$ Ni1	$\lvert 5\downarrow\rangle \to \lvert 21\downarrow\rangle$	57.46	772.006×10^{-3}	263.53	308.25	325.94	193.26	335.08	0.899	0.954
Spin-transfer	Ni3 $\to$ Ni1	$\lvert 7\uparrow\rangle \to \lvert 13\uparrow\rangle$	62.21	2.809×10^{-3}	65.55	81.09	22.21	116.93	433.04	2.776	0.994
Spin-transfer	Ni1 $\to$ Ni2	$\lvert 11\downarrow\rangle \to \lvert 8\downarrow\rangle$	75.68	1.708×10^{-3}	46.87	31.78	344.70	145.11	488.15	1.558	1.000
Spin-transfer	Ni1 $\to$ Ni3	$\lvert 11\downarrow\rangle \to \lvert 14\downarrow\rangle$	75.52	2.081×10^{-3}	97.55	103.16	262.51	103.23	494.31	2.524	0.981
Spin-transfer	Ni1 $\to$ Ni2	$\lvert 11\downarrow\rangle \to \lvert 18\downarrow\rangle$	70.27	767.069×10^{-3}	225.94	79.95	225.58	284.52	426.11	0.907	1.035
Spin-transfer	Ni2 $\to$ Ni1	$\lvert 18\downarrow\rangle \to \lvert 5\downarrow\rangle$	69.02	769.877×10^{-3}	87.08	94.79	18.00	267.72	460.21	0.822	1.039
Spin-transfer	Ni2 $\to$ Ni3	$\lvert 18\downarrow\rangle \to \lvert 14\downarrow\rangle$	77.83	764.988×10^{-3}	271.90	204.19	234.73	357.80	456.62	0.986	0.957
Spin-transfer	Ni1 $\to$ Ni3	$\lvert 21\downarrow\rangle \to \lvert 5\downarrow\rangle$	50.60	772.006×10^{-3}	285.71	57.23	19.29	118.63	313.60	0.464	0.999
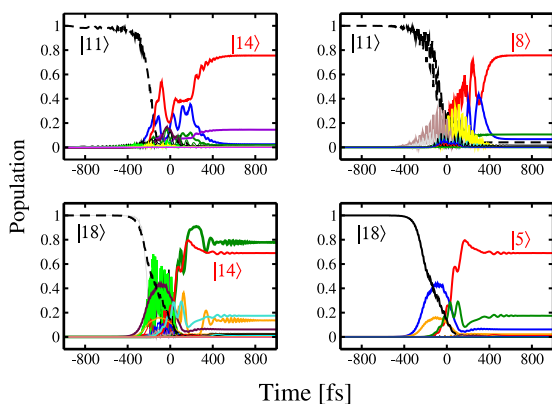
FIG. 15. Spin-down spin-transfer process $\lvert 11\rangle \to \lvert 14\rangle$ (Ni3 to Ni1), spin-down spin-transfer process $\lvert 11\rangle \to \lvert 8\rangle$ (Ni1 to Ni2), spin-down spin-transfer process $\lvert 18\rangle \to \lvert 14\rangle$ (Ni2 to Ni3), and spin-down spin-transfer process $\lvert 8\rangle \to \lvert 5\rangle$ (Ni3 to Ni3). The time-dependent population of the initial (black dashed line), final or target (red solid line), and intermediate (solid lines in different colors) states.

not fulfill the requirements (see Sec. III A) to achieve a spin-flip process.

Moreover, different spin-up and spin-down spin-transfer processes are accomplished. We present the fidelity of each process and the optimized parameters of the laser pulses in Table IV. We plot some of those spin-down spin-transfer processes in Fig. 15. For instance, we take $\lvert 11\downarrow\rangle$ and $\lvert 14\downarrow\rangle$ as initial and final states, respectively. At the many-body state $\lvert 11\downarrow\rangle$, the spin density is localized on Ni1, while at $\lvert 14\downarrow\rangle$, the spin density is localized on Ni3. The time-dependent population of each involved state is shown in Fig. 15. The fidelity of this process is 75.52%. By selecting the states $\lvert 18\rangle$ and $\lvert 14\rangle$ as initial and target states, respectively, we demonstrate that the spin density can be moved from Ni2 to Ni3 under a single laser pulse. The fidelity of this process reaches 77.83%. The optimized parameters of the laser pulse are $\theta = 271.90°$, $\phi = 204.19°$, $\gamma = 234.73°$, $\beta = 357.80°$, FWHM = 456.62 fs, and chirp = 0.957.

REFERENCES

[1] J. Chen, U. Bovensiepen, A. Eschenlohr, T. Müller, P. Elliott, E. K. U. Gross, J. K. Dewhurst, and S. Sharma, "Competing spin transfer and dissipation at Co/Cu(001) interfaces on femtosecond timescales," Phys. Rev. Lett. **122**, 067202 (2019).

[2] D. Chaudhuri, G. Lefkidis, and W. Hübner, "All-spin-based ultrafast nanologic elements with a Ni4 cluster," Phys. Rev. B **96**, 184413 (2017).

[3] H. Du, J. Liu, N. Zhang, J. Chang, W. Jin, C. Li, G. Lefkidis, and W. Hübner, "Theoretical study of laser-induced ultrafast spin dynamics in small iron-benzene clusters and of related laser and magnetic-field effects," Phys. Rev. B **99**, 134430 (2019).

[4] F. Liedy, R. Shi, M. Coletta, J. Vallejo, E. K. Brechin, G. Lefkidis, W. Hübner, and J. Olof Johansson, "Reprint of 'Photoinduced dynamics in an exchange-coupled trinuclear iron cluster,'" J. Magn. Magn. Mater. **502**, 166704 (2020).

[5] Y. Pavlyukh, E. Rentschler, H. J. Elmers, W. Hübner, and G. Lefkidis, "Broken symmetry states of metallacrowns: Distribution of spins and the g tensor," Phys. Rev. B **99**, 144418 (2019).

[6] L. Guo, X. Gu, X. Zhu, and X. Sun, "Recent advances in molecular spintronics: Multifunctional spintronic devices," Adv. Mater. **31**, 1805355 (2019).

[7] H. Shinohara, "Endohedral metallofullerenes," Rep. Prog. Phys. **63**, 843–892 (2000).

[8] A. A. Popov, S. Yang, and L. Dunsch, "Endohedral fullerenes," Chem. Rev. **113**, 5989–6113 (2013).

29 April 2024 13:08:03

[9] X. Lu, L. Feng, T. Akasaka, and S. Nagase, "Current status and future developments of endohedral metallofullerenes," Chem. Soc. Rev. **41**, 7723–7760 (2012).

[10] Q. Deng, T. Heine, S. Irle, and A. A. Popov, "Self-assembly of endohedral metallofullerenes: A decisive role of cooling gas and metal–carbon bonding," Nanoscale **8**, 3796–3808 (2016).

[11] A. Fallah, Y. Yonetani, R. Senga, K. Hirahara, R. Kitaura, H. Shinohara, and Y. Nakayama, "Thermal/electron irradiation assisted coalescence of $Sc_3N@C_{80}$ fullerene in carbon nanotube and evidence of charge transfer between pristine/coalesced fullerenes and nanotubes," Nanoscale **5**, 11755–11760 (2013).

[12] G. Lefkidis, G. P. Zhang, and W. Hübner, "Angular momentum conservation for coherently manipulated spin polarization in photoexcited NiO: An *ab initio* calculation," Phys. Rev. Lett. **103**, 217401 (2009).

[13] P. Baláž, K. Carva, U. Ritzmann, P. Maldonado, and P. M. Oppeneer, "Domain wall dynamics due to femtosecond laser-induced superdiffusive spin transport," Phys. Rev. B **101**, 174418 (2020).

[14] Y. S. Yordanov, D. R. M. Arvidsson-Shukur, and C. H. W. Barnes, "Efficient quantum circuits for quantum computational chemistry," Phys. Rev. A **102**, 062612 (2020).

[15] J. F. Gonthier, M. D. Radin, C. Buda, E. J. Doskocil, C. M. Abuan, and J. Romero, "Measurements as a roadblock to near-term practical quantum advantage in chemistry: Resource analysis," Phys. Rev. Res. **4**, 033154 (2022).

[16] D. Wang, O. Higgott, and S. Brierley, "Accelerated variational quantum eigensolver," Phys. Rev. Lett. **122**, 140504 (2019).

[17] H.-Y. Huang, R. Kueng, and J. Preskill, "Information-theoretic bounds on quantum advantage in machine learning," Phys. Rev. Lett. **126**, 190505 (2021).

[18] A. Mazzolo and C. Monthus, "Nonequilibrium diffusion processes via non-Hermitian electromagnetic quantum mechanics with application to the statistics of entropy production in the Brownian gyrator," Phys. Rev. E **107**, 014101 (2023).

[19] K. S. U. Kansanen, "Theory for polaritonic quantum tunneling," Phys. Rev. B **107**, 035405 (2023).

[20] P. W. Anderson, "Antiferromagnetism. Theory of superexchange interaction," Phys. Rev. **79**, 350–356 (1950).

[21] J. B. Goodenough, "An interpretation of the magnetic properties of the perovskite-type mixed crystals $La_{1-x}Sr_xCoO_{3-\lambda}$," J. Phys. Chem. Solids **6**, 287–297 (1958).

[22] J. Kanamori, "Superexchange interaction and symmetry properties of electron orbitals," J. Phys. Chem. Solids **10**, 87–98 (1959).

[23] W. Hübner, G. Lefkidis, C. D. Dong, D. Chaudhuri, L. Chotorlishvili, and J. Berakdar, "Spin-dependent Otto quantum heat engine based on a molecular substance," Phys. Rev. B **90**, 024401 (2014).

[24] B. Koopmans, J. J. M. Ruigrok, F. D. Longa, and W. J. M. de Jonge, "Unifying ultrafast magnetization dynamics," Phys. Rev. Lett. **95**, 267207 (2005).

[25] R. Gómez-Abal, O. Ney, K. Satitkovitchai, and W. Hübner, "All-optical subpicosecond magnetic switching in NiO(001)," Phys. Rev. Lett. **92**, 227402 (2004).

[26] C. P. Koch, U. Boscain, T. Calarco, G. Dirr, S. Filipp, S. J. Glaser, R. Kosloff, S. Montangero, T. Schulte-Herbrüggen, D. Sugny, and F. K. Wilhelm, "Quantum optimal control in quantum technologies. Strategic report on current status, visions and goals for research in Europe," EPJ Quantum Technol. **9**, 19 (2022).

[27] S. J. Glaser, U. Boscain, T. Calarco, C. P. Koch, W. Köckenberger, R. Kosloff, I. Kuprov, B. Luy, S. Schirmer, T. Schulte-Herbrüggen, D. Sugny, and F. K. Wilhelm, "Training Schrödinger's cat: Quantum optimal control," Eur. Phys. J. D **69**, 279 (2015).

[28] N. Ofek, A. Petrenko, R. Heeres, P. Reinhold, Z. Leghtas, B. Vlastakis, Y. Liu, L. Frunzio, S. M. Girvin, L. Jiang, M. Mirrahimi, M. H. Devoret, and R. J. Schoelkopf, "Extending the lifetime of a quantum bit with error correction in superconducting circuits," Nature **536**, 441–445 (2016).

[29] R. W. Heeres, P. Reinhold, N. Ofek, L. Frunzio, L. Jiang, M. H. Devoret, and R. J. Schoelkopf, "Implementing a universal gate set on a logical qubit encoded in an oscillator," Nat. Commun. **8**, 94 (2017).

[30] X. Wu, S. L. Tomarken, N. A. Petersson, L. A. Martinez, Y. J. Rosen, and J. L. DuBois, "High-fidelity software-defined quantum logic on a superconducting qudit," Phys. Rev. Lett. **125**, 170502 (2020).

[31] M. Werninghaus, D. J. Egger, F. Roy, S. Machnes, F. K. Wilhelm, and S. Filipp, "Leakage reduction in fast superconducting qubit gates via optimal control," npj Quantum Inf. **7**, 14 (2021).

[32] Y. Zhang, J. Liu, C. Li, W. Jin, G. Lefkidis, and W. Hübner, "Strain-promoted reversible spin transfer in rhombic graphene nanoflakes," Appl. Surf. Sci. **558**, 149770 (2021).

[33] Y. Zhang, J. Liu, C. Li, W. Jin, G. Lefkidis, and W. Hübner, "Strain-modulated ultrafast magneto-optic dynamics of graphene nanoflakes decorated with transition-metal atoms," Chin. Phys. B **30**, 097702 (2021).

[34] S. Sold, B. C. Mummaneni, N. C. Michenfelder, Y. Peng, A. K. Powell, A.-N. Unterreiner, G. Lefkidis, and W. Hübner, "Experimental and theoretical study of the ultrafast dynamics of a Ni_2Dy_2-compound in DMF after UV/Vis photoexcitation," ChemistryOpen **11**, e202100153 (2022).

[35] B. C. Mummaneni, J. Liu, G. Lefkidis, and W. Hübner, "Laser-controlled implementation of controlled-NOT, hadamard, SWAP, and pauli gates as well as generation of bell states in a 3d–4f molecular magnet," J. Phys. Chem. Lett. **13**, 2479–2485 (2022).

[36] C. Li, J. Liu, S. Zhang, G. Lefkidis, and W. Hübner, "Strain effect on the ultrafast spin switching of cobalt-doped carbon fullerenes," IEEE Trans. Magn. **51**, 2900505 (2015).

[37] S. Xu, Y. Zhang, R. Huang, J. Liu, W. Jin, G. Lefkidis, W. Hübner, and C. Li, "Strain manipulation of the local spin flip on $Ni@B_{80}$ endohedral fullerene," Phys. Chem. Chem. Phys. **23**, 25712–25719 (2021).

[38] C. Tan, J. Lee, S. G. Jung, T. Park, S. Albarakati, J. Partridge, M. R. Field, D. G. McCulloch, L. Wang, and C. Lee, "Hard magnetic properties in nanoflake van der Waals Fe_3GeTe_2," Nat. Commun. **9**, 1554 (2018).

[39] A. A. Khudorozhkov, P. N. Skirdkov, K. A. Zvezdin, P. M. Vetoshko, and A. F. Popkov, "Spin-torque diode frequency tuning via soft exchange pinning of both magnetic layers," Phys. Rev. B **96**, 214410 (2017).

[40] W. Hübner, S. Kersten, and G. Lefkidis, "Optical spin manipulation for minimal magnetic logic operations in metallic three-center magnetic clusters," Phys. Rev. B **79**, 184431 (2009).

[41] D. Chaudhuri, H. P. Xiang, G. Lefkidis, and W. Hübner, "Laser-induced ultrafast spin dynamics in di-tri- and tetranuclear nickel clusters, and the M process," Phys. Rev. B **90**, 245113 (2014).

[42] G. Akhgar, D. L. Creedon, L. H. Willems van Beveren, A. Stacey, D. I. Hoxley, J. C. McCallum, L. Ley, A. R. Hamilton, and C. I. Pakes, "G-factor and well width variations for the two-dimensional hole gas in surface conducting diamond," Appl. Phys. Lett. **112**, 042102 (2018).

[43] J. Liu, C. Li, W. Jin, G. Lefkidis, and W. Hübner, "Long-distance ultrafast spin transfer over a zigzag carbon chain structure," Phys. Rev. Lett. **126**, 037402 (2021).

[44] J. Liu, Y. Zhang, C. Li, W. Jin, G. Lefkidis, and W. Hübner, "Controllable spin-dynamic scenarios on zigzag carbon cross structure," Phys. Rev. B **106**, 094401 (2022).

[45] X. Liang, J. Yang, Y. Zhang, J. Liu, C. Li, G. Lefkidis, W. Hübner, and W. Jin, "A theoretical study of laser-induced ultrafast spin dynamics in trigonal monopyramidal iron and nickel complexes," Phys. Chem. Chem. Phys. **24**, 24881–24891 (2022).

[46] N. Zhang, H. Du, J. Chang, W. Jin, C. Li, G. Lefkidis, and W. Hübner, "*Ab initio* study of ultrafast laser-induced spin flip, spin-flip transfer, and spin crossover in $Co_mBz_n^{+/0}$ clusters ($m, n = 1, 2$)," Phys. Rev. B **98**, 104431 (2018).

[47] S. T. Akin, V. Zamudio-Bayer, K. Duanmu, G. Leistner, K. Hirsch, C. Bülow, A. Ławicki, A. Terasaki, B. von Issendorff, D. G. Truhlar, J. T. Lau, and M. A. Duncan, "Size-dependent ligand quenching of ferromagnetism in Co_3(benzene)$_n^+$ clusters studied with X-ray magnetic circular dichroism spectroscopy," J. Phys. Chem. Lett. **7**, 4568–4575 (2016).

[48] I. S. Youn, D. Y. Kim, N. J. Singh, S. W. Park, J. Youn, and K. S. Kim, "Intercalation of transition metals into stacked benzene rings: A model study of the intercalation of transition metals into bilayered graphene," J. Chem. Theory Comput. **8**, 99–105 (2012).

[49] R. Flores and M. Castro, "Stability of one- and two-layers $[TM(Benzene)_m]^{\pm 1}$, $m \leq 3$; TM = Fe, Co, and Ni, complexes," J. Mol. Struct. **1125**, 47–62 (2016).

[50] K. S. Kjær, W. Zhang, R. Alonso-Mori, U. Bergmann, M. Chollet, R. G. Hadt, R. W. Hartsock, T. Harlang, T. Kroll, K. Kubiček, H. T. Lemke, H. W. Liang, Y. Liu, M. M. Nielsen, J. S. Robinson, E. I. Solomon, D. Sokaras, T. B. van

Driel, T.-C. Weng, D. Zhu, P. Persson, K. Wärnmark, V. Sundström, and K. J. Gaffney, "Ligand manipulation of charge transfer excited state relaxation and spin crossover in [Fe(2,2′-bipyridine)$_2$(CN)$_2$]," Struct. Dyn. **4**, 044030 (2017).

[51] G. Lefkidis and W. Hübner, "*Ab initio* treatment of optical second harmonic generation in NiO," Phys. Rev. Lett. **95**, 077401 (2005).

[52] S. X. Wang, J. Labaziewicz, Y. Ge, R. Shewmon, and I. L. Chuang, "Demonstration of a quantum logic gate in a cryogenic surface-electrode ion trap," Phys. Rev. A **81**, 062332 (2010).

[53] S. Bellucci and P. Onorato, "Quantum wires as logic operators: XNOR and NOR gate response in a ballistic interferometer," Phys. Rev. B **81**, 165427 (2010).

[54] L.-A. Wu, D. A. Lidar, and M. Friesen, "One-spin quantum logic gates from exchange interactions and a global magnetic field," Phys. Rev. Lett. **93**, 030501 (2004).

[55] W. Jin, F. Rupp, K. Chevalier, M. M. N. Wolf, M. C. Rojas, G. Lefkidis, H.-J. Krüger, R. Diller, and W. Hübner, "Combined theoretical and experimental study of spin and charge dynamics on the homodinuclear complex [Ni$_2^{II}$(L-N$_4$Me$_2$)(emb)]," Phys. Rev. Lett. **109**, 267209 (2012).

[56] G. P. Zhang and W. Hübner, "Laser-induced ultrafast demagnetization in ferromagnetic metals," Phys. Rev. Lett. **85**, 3025–3028 (2000).

[57] Y.-R. Lin, S. Wolff, P. Schädlich, M. Hutter, S. Soubatch, T.-L. Lee, F. S. Tautz, T. Seyller, C. Kumpf, and F. C. Bocquet, "Vertical structure of Sb-intercalated quasifreestanding graphene on SiC(0001)," Phys. Rev. B **106**, 155418 (2022).

[58] P. L. de Andres, R. Ramírez, and J. A. Vergés, "Strong covalent bonding between two graphene layers," Phys. Rev. B **77**, 045403 (2008).

[59] J. T. Titantah and D. Lamoen, "Energy-loss near-edge structure changes with bond length in carbon systems," Phys. Rev. B **72**, 193104 (2005).

[60] A. Van Orden and R. J. Saykally, "Small carbon clusters: Spectroscopy, structure, and energetics," Chem. Rev. **98**, 2313–2358 (1998).

[61] L. Horný, N. D. K. Petraco, and H. F. Schaefer, "Odd carbon long linear chains HC$_{2n+1}$H (n = 4–11): Properties of the neutrals and radical anions," J. Am. Chem. Soc. **124**, 14716–14720 (2002).

[62] H. Ding, T. W. Schmidt, T. Pino, A. E. Boguslavskiy, F. Güthe, and J. P. Maier, "Gas phase electronic spectra of the linear carbon chains HC$_{2n+1}$H (n = 3–6, 9)," J. Chem. Phys. **119**, 814–819 (2003).

[63] M. J. Travers, M. C. McCarthy, C. A. Gottlieb, and P. Thaddeus, "Laboratory detection of the ring-chain molecule C$_5$H$_2$," Astrophys. J. **483**, L135 (1997).

[64] N. K and C. S. Rout, "Conducting polymers: A comprehensive review on recent advances in synthesis, properties and applications," RSC Adv. **11**, 5659 (2021).

[65] D. Khokhriakov, B. Karpiak, A. M. Hoque, and S. P. Dash, "Two-dimensional spintronic circuit architectures on large scale graphene," Carbon **161**, 892–899 (2020).

[66] W. X. Zhang, C. H. Shi, C. He, and M. Bai, "External-strain induced transition from Schottky to ohmic contact in graphene/InS and graphene/Janus In$_2$SSe heterostructures," J. Solid State Chem. **289**, 121511 (2020).

[67] S. Mishra, D. Beyer, K. Eimre, S. Kezilebieke, R. Berger, O. Gröning, C. A. Pignedoli, K. Müllen, P. Liljeroth, P. Ruffieux, X. Feng, and R. Fasel, "Topological frustration induces unconventional magnetism in a nanographene," Nat. Nanotechnol. **15**, 22 (2020).

[68] N. Sethulakshmi, A. Mishra, P. Ajayan, Y. Kawazoe, A. K. Roy, A. K. Singh, and C. S. Tiwary, "Magnetism in two-dimensional materials beyond graphene," Mater. Today **27**, 107 (2019).

[69] T. Hartenstein, C. Li, G. Lefkidis, and W. Hübner, "Local light-induced spin manipulation in two magnetic centre metallic chains," J. Phys. D: Appl. Phys. **41**, 164006 (2008).

[70] S. Wang, Q. Sun, O. Gröning, R. Widmer, C. A. Pignedoli, L. Cai, X. Yu, B. Yuan, C. Li, H. Ju, J. Zhu, P. Ruffieux, R. Fasel, and W. Xu, "On-surface synthesis and characterization of individual polyacetylene chains," Nat. Chem. **11**, 924 (2019).

[71] C. Fredriksson and J. L. Brédas, "Metal/conjugated polymer interfaces: A theoretical investigation of the interaction between aluminum and trans-polyacetylene oligomers," J. Chem. Phys. **98**, 4253 (1993).

[72] *Modern Acetylene Chemistry*, edited by P. J. Stang and F. Diederich (Wiley, New York, 2008).

[73] M. R. Bryce, "A review of functional linear carbon chains (oligoynes, polyynes, cumulenes) and their applications as molecular wires in molecular electronics and optoelectronics," J. Mater. Chem. C **9**, 10524 (2021).

[74] T. Yamamoto, K. Kobayashi, T. Yasuda, Z.-H. Zhou, I. Yamaguchi, T. Ishikawa, and S.-y. Koshihara, "Preparation of polyacetylenes via organometallic C-C coupling reactions," Polym. Bull. **52**, 315 (2004).

[75] T. Yamamoto, K. Ohya, K. Kobayashi, K. Okamoto, S. Koie, H. Fukumoto, T.-a. Koizumi, and I. Yamaguchi, "Preparation of head-to-head type substituted polyacetylenes by organometallic polycondensation," Macromolecules **42**, 3207 (2009).

[76] T. Masuda, "Substituted polyacetylenes," J. Polym. Sci., Part A: Polym. Chem. **45**, 165–180 (2007).

[77] A. F. Lashua, T. M. Smith, H. Hu, L. Wei, D. G. Allis, M. B. Sponsler, and B. S. Hudson, "Commensurate urea inclusion crystals with the guest (E,E)-1,4-diiodo-1,3-butadiene," Cryst. Growth Des. **13**, 3852 (2013).

[78] S. A. Dincă, D. Allis, A. Lashua, M. Sponsler, and B. Hudson, "Insulated polyacetylene chains in an inclusion complex by photopolymerization," MRS Proc. **1799**, 7 (2015).

[79] S. A. Dincă, D. G. Allis, M. D. Moskowitz, M. B. Sponsler, and B. S. Hudson, "Preparation of ordered polyacetylene by solid-state polymerization in nanoscale confinement," Chem. Mater. **32**, 1769 (2020).

[80] J. Li, S. Sanz, J. Castro-Esteban, M. Vilas-Varela, N. Friedrich, T. Frederiksen, D. Peña, and J. I. Pascual, "Uncovering the triplet ground state of triangular graphene nanoflakes engineered with atomic precision on a metal surface," Phys. Rev. Lett. **124**, 177201 (2020).

[81] Y. Ge, L. Chen, C. Jiang, J. Ji, Q. Tan, D. Pan, W. Zhang, R. Zhang, E. Janzen, J. H. Edgar, S. Sang, and H. Wang, "Edge magnetism of triangular graphene nanoflakes embedded in hexagonal boron nitride," Carbon **203**, 59–67 (2023).

[82] S. Bittner, B. Dietz, M. Miski-Oglu, P. Oria Iriarte, A. Richter, and F. Schäfer, "Observation of a Dirac point in microwave experiments with a photonic crystal modeling graphene," Phys. Rev. B **82**, 014301 (2010).

[83] R. J. Bartlett and G. D. Purvis, "Many-body perturbation theory, coupled-pair many-electron theory, and the importance of quadruple excitations for the correlation problem," Int. J. Quantum Chem. **14**, 561–581 (1978).

[84] J. A. Pople, R. Krishnan, H. B. Schlegel, and J. S. Binkley, "Electron correlation theories and their application to the study of simple reaction potential surfaces," Int. J. Quantum Chem. **14**, 545–560 (1978).

[85] G. D. Purvis and R. J. Bartlett, "A full coupled-cluster singles and doubles model: The inclusion of disconnected triples," J. Chem. Phys. **76**, 1910–1918 (1982).

[86] J. F. Stanton and R. J. Bartlett, "The equation of motion coupled-cluster method. A systematic biorthogonal approach to molecular excitation energies, transition probabilities, and excited state properties," J. Chem. Phys. **98**, 7029–7039 (1993).

[87] M. W. Schmidt, K. K. Baldridge, J. A. Boatz, S. T. Elbert, M. S. Gordon, J. H. Jensen, S. Koseki, N. Matsunaga, K. A. Nguyen, S. Su, T. L. Windus, M. Dupuis, and J. A. Montgomery, Jr., "General atomic and molecular electronic structure system," J. Comput. Chem. **14**, 1347–1363 (1993).

[88] G. Lefkidis and W. Hübner, "First-principles study of ultrafast magneto-optical switching in NiO," Phys. Rev. B **76**, 014418 (2007).

[89] M.-L. Xie, Y.-T. Zheng, J. Liu, W. Jin, C. Li, G. Lefkidis, and W. Hübner, "First-principles study of the electronic and magnetic properties of Fe, Co, and Ni dimers adsorbed on polycyclic-aromatic-hydrocarbon molecules as well as the laser chirp effect on the ultrafast spin dynamics," Phys. Rev. B **103**, 054433 (2021).

[90] P. Wang, M. Qiu, X. Lu, W. Jin, C. Li, G. Lefkidis, and W. Hübner, "First-principles study of spin properties and laser-induced ultrafast spin dynamics in transition-metal oxide clusters $TM_3O_3^{0/+}$ (TM = Fe, Co, and Ni)," Phys. Rev. B **101**, 104414 (2020).

[91] W. Jin, C. Li, G. Lefkidis, and W. Hübner, "Laser control of ultrafast spin dynamics on homodinuclear iron- and nickel-oxide clusters," Phys. Rev. B **89**, 024419 (2014).

[92] J. R. Cash and A. H. Karp, "A variable order Runge-Kutta method for initial value problems with rapidly varying right-hand sides," ACM Trans. Math. Software **16**, 201–222 (1990).

[93] K. Koshihara and K. Yuasa, "Quantum ergotropy and quantum feedback control," Phys. Rev. E **107**, 064109 (2023).

[94] P. Mehta, M. Bukov, C.-H. Wang, A. G. R. Day, C. Richardson, C. K. Fisher, and D. J. Schwab, "A high-bias, low-variance introduction to machine learning for physicists," Phys. Rep. **810**, 1–124 (2019).

29 April 2024 13:08:03

[95] G. Lefkidis, "Chap. Ultrafast laser dynamics on molecular nanomagnets," in *Nanoscience and Computational chemistry: Research Progress*, edited by A. G. Mercader, E. A. Castro, and A. K. Haghi (Apple Academic Press, 2013).

[96] R. Porotti, V. Peano, and F. Marquardt, "Gradient ascent pulse engineering with feedback," PRX Quantum 4, 030305 (2023).

[97] S. S. Gregersen, S. R. Power, and A.-P. Jauho, "Nanostructured graphene for spintronics," Phys. Rev. B **95**, 121406 (2017).

[98] M. G. Zeng, L. Shen, Y. Q. Cai, Z. D. Sha, and Y. P. Feng, "Perfect spin-filter and spin-valve in carbon atomic chains," Appl. Phys. Lett. **96**, 042104 (2010).

[99] D. Dutta, M. Becherer, D. Bellaire, F. Dietrich, M. Gerhards, G. Lefkidis, and W. Hübner, "Characterization of the isolated $[Co_3Ni(EtOH)]^+$ cluster by IR spectroscopy and spin-dynamics calculations," Phys. Rev. B **97**, 224404 (2018).

[100] H. Xiang, G. Lefkidis, and W. Hübner, "Unified theory of ultrafast femtosecond and conventional picosecond magnetic dynamics in the distorted three-center magnetic cluster Ni_3Na_2," Phys. Rev. B **86**, 134402 (2012).

[101] V. V. Dobrovitski, M. I. Katsnelson, and B. N. Harmon, "Mechanisms of decoherence in weakly anisotropic molecular magnets," Phys. Rev. Lett. **84**, 3458 (2000).

[102] C. Li, W. Jin, H. Xiang, G. Lefkidis, and W. Hübner, "Theory of laser-induced ultrafast magneto-optic spin flip and transfer in charged two-magnetic-center molecular ions: Role of bridging atoms," Phys. Rev. B **84**, 054415 (2011).

[103] P. Jakob, K. Anhut, S. Schnur, and A. Groß, "Monodisperse microisland formation on Ni/Ru(0001) monolayers," Phys. Rev. Lett. **101**, 206101 (2008).

[104] C. Li, J. Liu, G. Lefkidis, and W. Hübner, "Reversible ultrafast spin switching on $Ni@B_{80}$ endohedral fullerene," Phys. Chem. Chem. Phys. **19**, 673–680 (2017).

[105] F. Neese, T. Petrenko, D. Ganyushin, and G. Olbrich, "Advanced aspects of ab initio theoretical optical spectroscopy of transition metal complexes: Multiplets, spin-orbit coupling and resonance Raman intensities," Coord. Chem. Rev. **251**, 288–327 (2007), part of the Special Issue: Highlighting the Many Aspects of the Electronic Spectrosocpy of Inorganic Compounds.

[106] G. M. Cole and B. B. Garrett, "Atomic and molecular spin-orbit coupling constants for 3d transition metal ions," Inorg. Chem. **9**, 1898–1902 (1970).

[107] T. E. H. Walker and W. G. Richards, "Molecular spin–orbit coupling constants. The role of core polarization," J. Chem. Phys. **52**, 1311–1314 (1970).

[108] M. Nooijen and R. J. Bartlett, "Equation of motion coupled cluster method for electron attachment," J. Chem. Phys. **102**, 3629–3647 (1995).

[109] J. R. Gour, P. Piecuch, and M. Włoch, "Active-space equation-of-motion coupled-cluster methods for excited states of radicals and other open-shell systems: EA-EOMCCSDt and IP-EOMCCSDt," J. Chem. Phys. **123**, 134113 (2005).

[110] H. Weihe, H. U. Güdel, "Quantitative Interpretation of the Goodenough-Kanamori Rules: A Critical Analysis," Inorg. Chem. **36**, 3632 (1997).

[111] G. Lefkidis, W. Jin, J. Liu, D. Dutta, and W. Hübner, "Topological spin–charge gearbox on a real molecular magnet," J. Phys. Chem. Lett. **11**, 2592–2597 (2020).

[112] Q. Gu, X. Huang, J. Xi, and Z. Gao, "The influence of magnetic field on fatigue and mechanical properties of a 35CrMo steel," Metals **11**, 542 (2021).

[113] I. Urcelay-Olabarria, E. Ressouche, V. Y. Ivanov, V. Skumryev, Z. Wang, Y. Skourski, A. M. Balbashov, Y. F. Popov, G. P. Vorob'ev, N. Qureshi, J. L. García-Muñoz, and A. A. Mukhin, "Influence of the magnetic field on the stability of the multiferroic conical spin arrangement of $Mn_{0.80}Co_{0.20}WO_4$," Phys. Rev. B **98**, 134430 (2018).

[114] M. J. G. Peeters, Y. M. van Ballegooie, and B. Koopmans, "Influence of magnetic fields on ultrafast laser-induced switching dynamics in Co/Gd bilayers," Phys. Rev. B **105**, 014429 (2022).

[115] B. Gao, T. Chen, H. Yan, C. Duan, C.-L. Huang, X. P. Yao, F. Ye, C. Balz, J. R. Stewart, K. Nakajima, S. Ohira-Kawamura, G. Xu, X. Xu, S.-W. Cheong, E. Morosan, A. H. Nevidomskyy, G. Chen, and P. Dai, "Magnetic field effects in an octupolar quantum spin liquid candidate," Phys. Rev. B **106**, 094425 (2022).

[116] H. Qian, J. Guo, Z. Wei, and J. Liu, "Multicaloric effect in synergic magnetostructural phase transformation Ni-Mn-Ga-In alloys," Phys. Rev. Mater. **6**, 054401 (2022).

[117] G. D. Förster and L. J. Lewis, "Numerical study of double-pulse laser ablation of Al," Phys. Rev. B **97**, 224301 (2018).

[118] M. Mattern, J.-E. Pudell, G. Laskin, A. von Reppert, and M. Bargheer, "Analysis of the temperature- and fluence-dependent magnetic stress in laser-excited $SrRuO_3$," Struct. Dyn. **8**, 024302 (2021).

[119] E. Räsänen, A. Castro, J. Werschnik, A. Rubio, and E. K. U. Gross, "Coherent quantum switch driven by optimized laser pulses," Physica E **40**, 1593–1595 (2008).

[120] A. I. Krylov, "Equation-of-Motion coupled-cluster methods for open-shell and electronically excited species: The Hitchhiker's guide to Fock space," Annu. Rev. Phys. Chem. **59**, 433–462 (2008).

[121] K. B. Wiberg, A. E. de Oliveira, and G. Trucks, "A comparison of the electronic transition energies for ethene, isobutene, formaldehyde, and acetone calculated using RPA, TDDFT, and EOM-CCSD. Effect of basis sets," J. Phys. Chem. A **106**, 4192–4199 (2002).

[122] M. Caricato, G. W. Trucks, M. J. Frisch, and K. B. Wiberg, "Oscillator strength: How does TDDFT compare to EOM-CCSD?," J. Chem. Theory Comput. **7**, 456–466 (2011).

[123] M. Caricato, G. W. Trucks, M. J. Frisch, and K. B. Wiberg, "Electronic transition energies: A study of the performance of a large range of single reference density functional and wave function methods on valence and Rydberg states compared to experiment," J. Chem. Theory Comput. **6**, 370–383 (2010).

[124] B. Saha, M. Ehara, and H. Nakatsuji, "Investigation of the electronic spectra and excited-state geometries of poly(para-phenylene vinylene) (PPV) and poly(para-phenylene) (PP) by the symmetry-adapted cluster configuration interaction (SAC-CI) method," J. Phys. Chem. A **111**, 5473–5481 (2007).

[125] R. Fukuda and H. Nakatsuji, "Formulation and implementation of direct algorithm for the symmetry-adapted cluster and symmetry-adapted cluster–configuration interaction method," J. Chem. Phys. **128**, 094105 (2008).

[126] R. Fukuda, M. Ehara, and H. Nakatsuji, "Excited states and electronic spectra of extended tetraazaporphyrins," J. Chem. Phys. **133**, 144316 (2010).